5-2016

Effect of non-uniform air-side velocity distribution on heat transfer model predictions for microchannel condenser.

Zachary Chapin

EFFECT OF NON-UNIFORM AIR-SIDE VELOCITY DISTRIBUTION ON HEAT TRANSFER MODEL PREDICTIONS FOR MICROCHANNEL CONDENSERS

By
Zachary Chapin
B.S., University of Michigan, 2012

A Thesis
Submitted to the Faculty of the
University of Louisville
J.B. Speed School of Engineering
In Partial Fulfillment of the Requirements
For the Degree of

Master of Science in Mechanical Engineering

Department of Mechanical Engineering
University of Louisville
Louisville, KY

May 2016

EFFECT OF NON-UNIFORM AIR-SIDE VELOCITY DISTRIBUTION ON HEAT TRANSFER MODEL PREDICTIONS FOR MICROCHANNEL CONDENSERS

Submitted by:

Zachary Chapin
B.S., University of Michigan, 2012

A Thesis Approved On

April 18, 2016

By the Following Examination Committee:

_____
Dr. Ellen Brehob, Thesis Co-director

_____
Dr. Sam Park, Thesis Co-director

_____
Dr. Andrea Kelecy

_____
Dr. Gerold Willing

ACKNOWLEDGEMENTS

I would like to thank my advisors Dr. Brehob, Dr. Park and Dr. Kelecy for their guidance and help throughout this project. My special thanks to Brent Junge, Mike Kempiak, Erik Hitzelberger, Carlos Herrera and Avi Patil for their knowledge and expertise in this area of study. Also, my gratitude goes to Tim Oconnell and Scott Welham for encouraging and enabling me to do this research.

ABSTRACT

EFFECT OF NON-UNIFORM AIR-SIDE VELOCITY DISTRIBUTION ON HEAT TRANSFER MODEL PREDICITONS FOR MICROCHANNEL CONDENSERS

Zachary Chapin

April 18, 2016

This is a study of the effects on heat transfer capacity predictions of microchannel condensers when airflow is maldistributed due to the shape of the condenser. The three shapes investigated in this study are flat, U-shape and roll. Each coil was tested in a water calorimeter and those results were compared to the model prediction. The model prediction was calculated using CoilDesigner™ modeling software with standard correlations. Using the uniform airflow assumption, the model over predicted the heat capacity measured in the calorimeter by 5-11% depending on the coil and inlet conditions. The local airflow velocity was measured using a vane anemometer, particle image velocimetry and a hotwire anemometer depending on the method that suited a particular geometry. The measured airflow profile was applied to the model and the heat capacity prediction error was reduced by 0.5-1.5%.

TABLE OF CONTENTS

LIST OF TABLES

LIST OF FIGURES

1 INTRODUCTION

Heat exchangers have a long history in the field of thermodynamics and heat transfer, affecting industries from transportation and power generation to refrigeration and air conditioning. Heat exchangers are a critical component in a thermodynamic cycle where heat is removed or added to the surrounding environment. As such, heat exchangers are tuned for specific applications and are often the limiting factor in a system design.

The topic of this paper revolves around a particular type of heat exchanger, a microchannel heat exchanger (MCHX), shown in Figure 1.1, in a condenser application. For the sake of simplicity it is easiest to compare a MCHX to a typical fin-and-tube heat exchanger. There are many benefits that the MCHX boasts over the fin and tube heat exchanger. MCHX manufacturers claim improvements in charge, size, efficiency, pressure drop and corrosion (Khan & Fartaj, 2011). The efficiency increase in MCHXs yield reductions in charge and size of HXs while holding heat transfer capacity constant. The corrosion performance is improved because the coils can be made 100% from aluminum which eliminates galvanic corrosion failures within the heat exchanger. Aluminum is also much less dense than copper or steel which could return a significant weight savings, as much as 70%.

Figure 1.1: Example of a microchannel heat exchanger

MCHXs have been used in the automotive industry for years but more recently have been researched for applications in other fields like consumer and industrial air conditioning. The goal of this paper is to increase the ability of MCHXs to be used more broadly by studying the effects of airflow maldistribution on model predictions brought about by uniquely shaped heat exchangers and different airflow directions. Airflow maldistribution refers to an uneven distribution across the face of HX as a whole. The term maldistribution has a negative connotation associated with it but is suitable for discussing heat exchangers because maldistribution of airflow has a negative impact on overall HX efficiency. This work should aid in understanding as it pertains to designing uniquely shaped MCHXs for new applications.

2 BACKGROUND

There have been many papers published that pertain to MCHX heat transfer and a few address the issue of maldistribution but mostly on the refrigerant side. In this section basic analysis and relevant literature will be discussed to understand MCHX benefits, previous studies and heat transfer correlations and models.

2.1 Past and Present Studies

A majority of the work done pertaining to maldistribution and MCHXs is in the area of refrigerant maldistribution in the headers and tubes. This is clearly a critical component in the design of the MCHX; if there is little refrigerant flow the tube effectiveness decreases significantly since no heat transfer can occur. The present study doesn't consider the effects of refrigerant maldistribution.

A study being done currently through Florida International University could have a bearing on this study. Stated in Section 2.3, the current correlations for this type of MCHX construction apply to higher air side Reynolds numbers than those looked at in this experiment. The work being done currently is to develop a new correlation for low air side Reynolds numbers. This study could be updated assuming that correlation proves to be valid. It is expected to show however, that the results for the present study were valid despite being outside the range recommended for the correlation used.

Airflow maldistribution has been studied by The Sustainable Thermal Systems Laboratory at the Georgia Institute of Technology (2014). Using the ε-NTU method they determined for a linearly maldistributed airflow of 50% the mass of the condenser had to increase by 7% to maintain heat duty. They also optimized the maldistributed condition by using a fin density distribution. Fin density was increased in areas of lower airflow and decreased in areas of higher airflow. The result reduced the mass of the condenser by 3% while maintaining the same performance as the baseline in maldistributed airflow.

Huang et al. (2014a) developed the model used in this study to predict the performance of the MCHX with variable geometries and inlet conditions i.e. airflow maldistribution. In a follow up paper Huang et al. (2014b) optimized a MC condenser that has a linearly maldistributed airflow. Using variable fin spacing and tube geometry the coil was optimized to reduce the mass by 19% while maintaining similar heat capacity.

2.2 Basic Analysis

As defined by London (1980), "A compact heat exchanger incorporates a heat transfer surface having a high area density. That is a high heat-transfer surface-to-volume ratio." Compact heat exchangers are those that have a surface area density greater than 122 ft^2/ft^3 where area density, α, is defined by Equation [2-1]. In comparison, shell and tube heat exchangers are on the order of 30 ft^2/ft^3 (Shah & Sekulic, 2003).

$$\alpha = \frac{A}{\forall} \qquad \textbf{[2-1]}$$

High surface area density is one factor that allows heat exchangers to be smaller and maintain capacity. Surface area density can be substituted into the heat exchanger equation for overall heat transfer coefficient, U. Equation [2-2] shows how increasing the surface area density can allow a decrease in heat exchanger volume while maintaining heat transfer rate, q.

$$q = UA\Delta\mathrm{T} = U\alpha\forall\Delta\mathrm{T} \qquad \textbf{[2-2]}$$

A theoretical analysis of a MCHX can be represented using a thermal resistance network shown in Figure 2.1. This network has three main components; thermal resistance due to the refrigerant, tubes and air. The air resistance term is a function of the heat transfer coefficient and fin efficiency, which is also a function of the heat transfer coefficient. Compared to the other two terms the tube resistance will be very small, having little effect on the performance of this type of HX. According to Khan and Fartaj (2011) the airside can account for more than 80% of the total resistance so small changes in the airflow could account for large discrepancies in results when modeling a system. Refrigerant flow in a channel is well defined for single phase flow. The airside heat transfer coefficient for a MCHX with louver fins has been studied extensively but comes with higher inaccuracy.

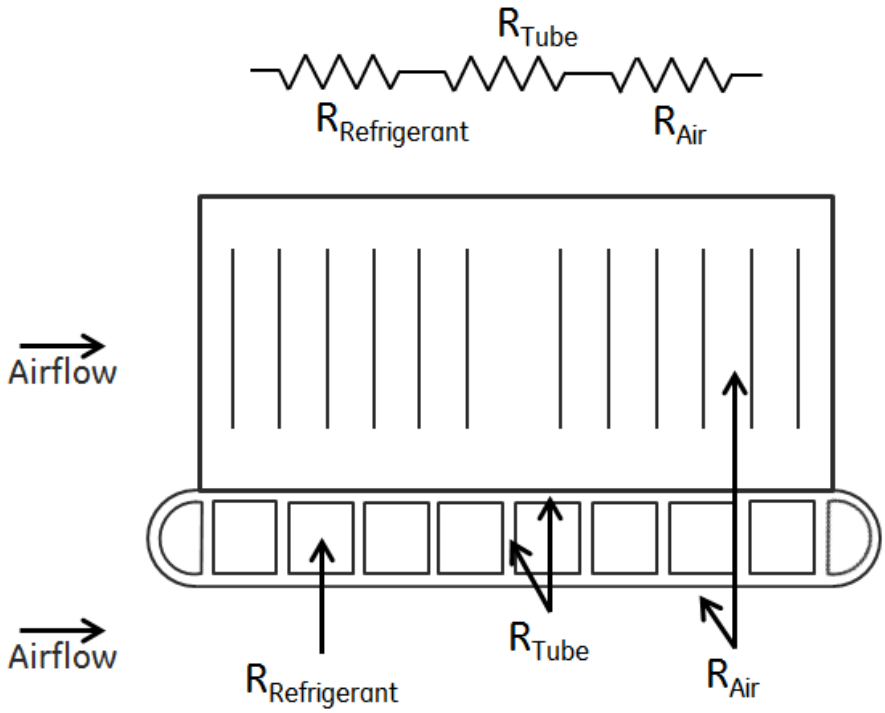

Figure 2.1: MCHX diagram showing thermal resistances and thermal resistance network

2.3 Chang and Wang Louver Fin Correlation

Until 1997 correlations for louvered fin MCHXs were developed for specific geometries. Correlations for triangular fin channels, rectangular fin channels and fins with splitter plates each had their own correlations. Chang and Wang (1997) developed a correlation that could be used to apply to all of these geometries. The correlation they developed is shown in Equation [2-3]. Some of these variables are shown defined in Figure 2.3.

$$j = Re_{Lp}{}^{-0.49}\left(\frac{\theta}{90}\right)^{0.27}\left(\frac{F_p}{L_p}\right)^{-0.14}\left(\frac{F_l}{L_p}\right)^{-0.29}\left(\frac{T_d}{L_p}\right)^{-0.23}\left(\frac{L_l}{L_p}\right)^{0.68}\left(\frac{T_p}{L_p}\right)^{-0.28}\left(\frac{t_f}{L_p}\right)^{-0.05} \quad \textbf{[2-3]}$$

θ	F_p	L_p	T_d	L_l	T_p	t_f
Louver Angle	Fin Pitch	Louver Pitch	Tube Depth	Louver Length	Tube Pitch	Fin Thickness

To verify this correlation 91 data points were used from eight previous studies of specific geometries used by those who developed the previous correlations. Some of the previous correlations were done by Achaichia and Cowell (1988), Webb and Jung (1992), and Sunden and Svantesson (1992) to name a few. Almost 90% of the data points were shown to fall within ±15%. The next best correlation at that time predicted about 74% within ±15%. The Chang and Wang correlation was developed for $100 < Re_{Lp} < 3000$. The Reynolds number is of particular interest in this study because the airflow rates studied are very low, thus have low Reynolds numbers which fall below the limit recommended for this correlation.

2.4 CoilDesigner™

CoilDesigner™ (CEEE, 2004-2016) is a heat exchanger modelling program developed through the Modeling and Optimization Consortium at the Center for Environmental Energy Engineering at the University of Maryland. This is a powerful program with a friendly user interface and uses the best heat transfer and pressure drop correlations available. This software allows quick optimization studies to be conducted. The software provides the ability to select different correlations and correction factors, choose all input conditions and modify coil circuiting easily with the user interface. One of the more recent features added to CoilDesigner™ is the MCHX modeling tool.

2.4.1 SETUP AND RESULTS

The CoilDesigner™ software easily navigates the process of creating a new coil to study. For this example the "Micro-channel Heat Exchanger, Using headers" construction was used. The program changes the information it requests based on the HX construction selected when a new coil is started. Once the solver and number of segments per tube are selected by the user, CoilDesigner™ asks for the tube and fin geometries as shown in Figure 2.2 and Figure 2.3. When the fin type is selected a diagram to show the parameters appears to help with the nomenclature.

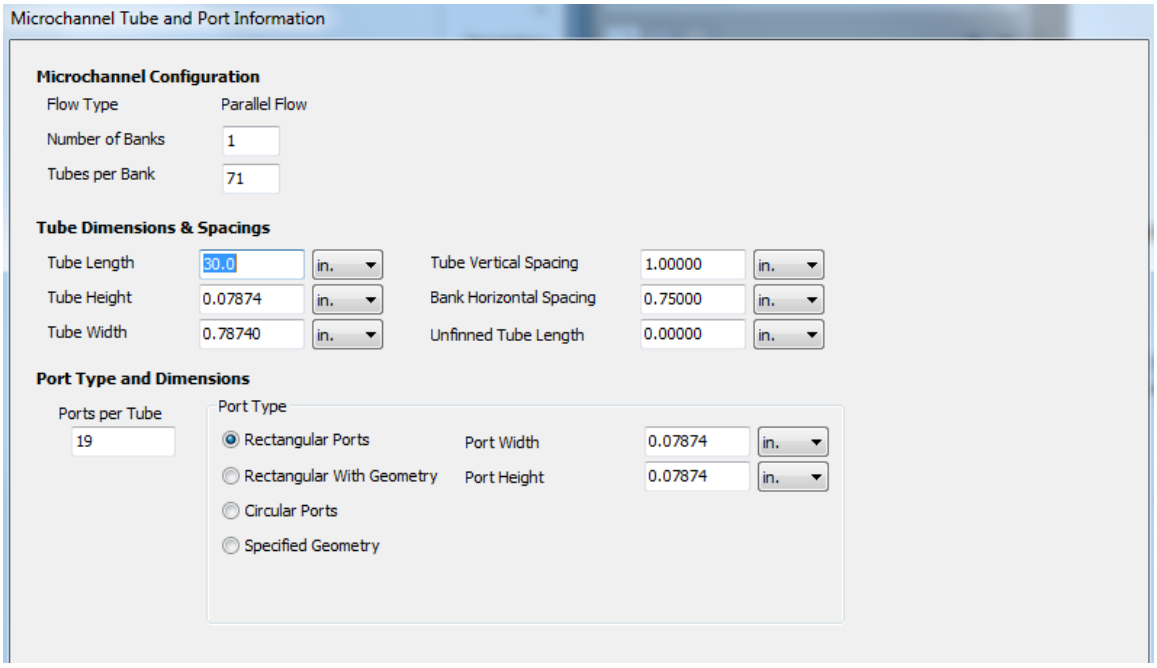

Figure 2.2: Tube geometry input screen in CoilDesigner™

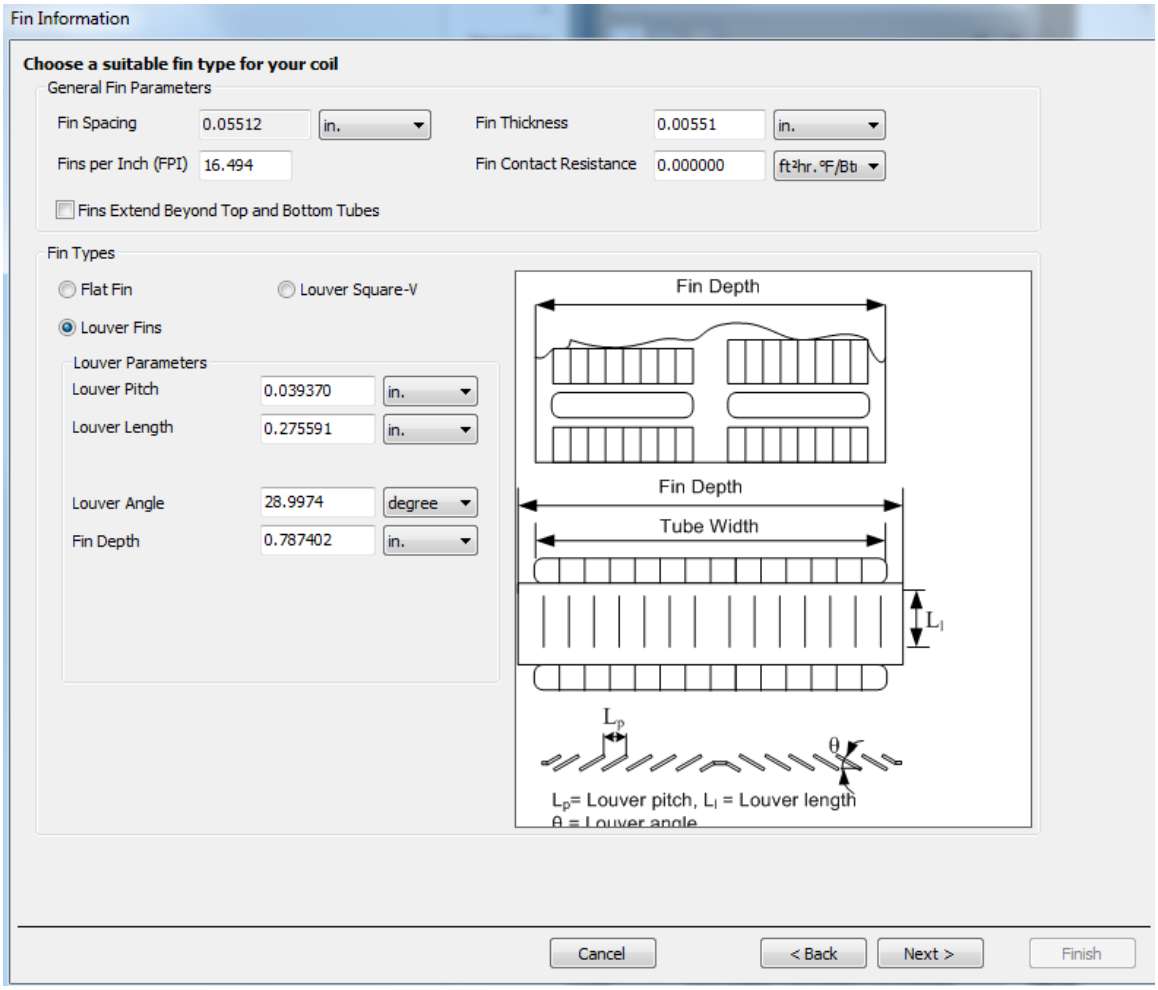

Figure 2.3: Fin geometry input screen in CoilDesigner™

Once the geometry has been set the working fluids can be selected. There are over 100 preloaded refrigerants to choose from or a unique fluid can be manually entered. Next, the heat transfer and pressure drop correlations for the air side, refrigerant liquid phase, refrigerant two phase and refrigerant vapor phase can be selected independently. There are many correlations preloaded into the software.

The overall construction is mostly finished at this point except for the microchannel pass arrangement. Under the project dropdown menu the microchannel passes and the

hydraulic diameter of the headers may be defined if they are present. Figure 2.4 shows the pass arrangement window for one of the constructions for this study.

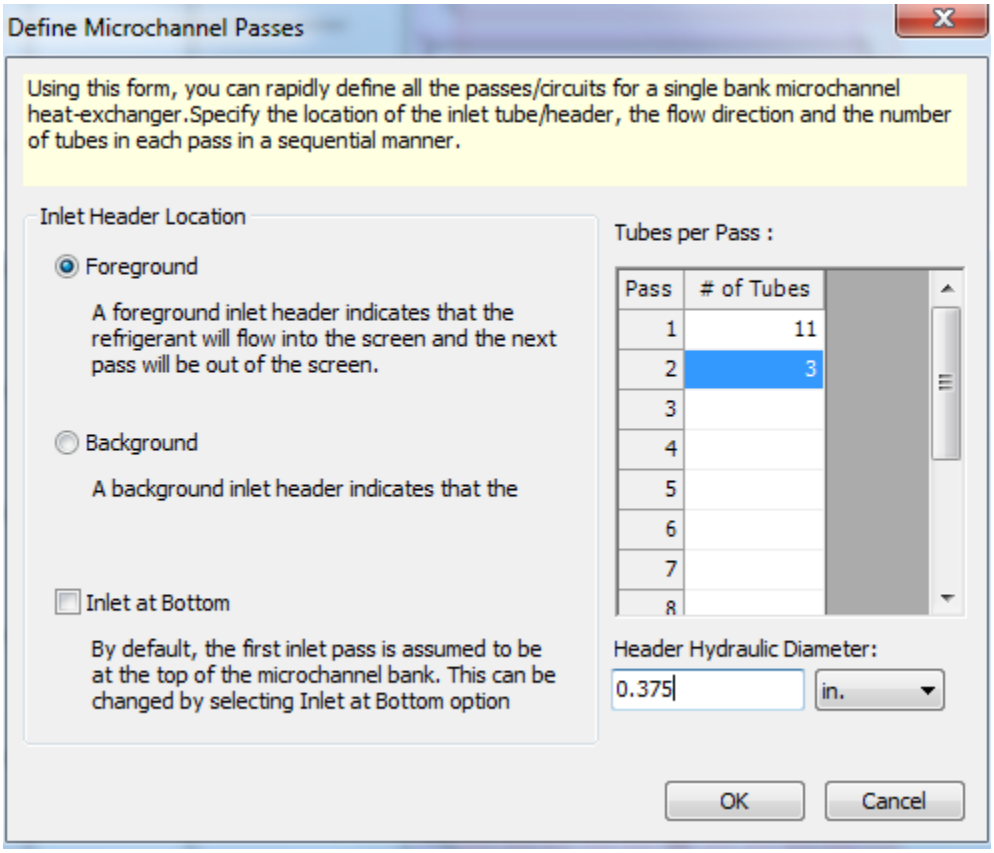

Figure 2.4: Pass arrangement window in CoilDesigner™

Shown in Figure 2.5 are the inlet conditions for the air and liquid that can be input by the user. Providing the airflow rate to the simulation automatically applies a uniform flow distribution across the face of the coil. The fluid state specification shown in Figure 2.5 has several options but to correspond to the testing done in this work, with liquid water on the refrigerant side, single phase refrigerant is appropriate.

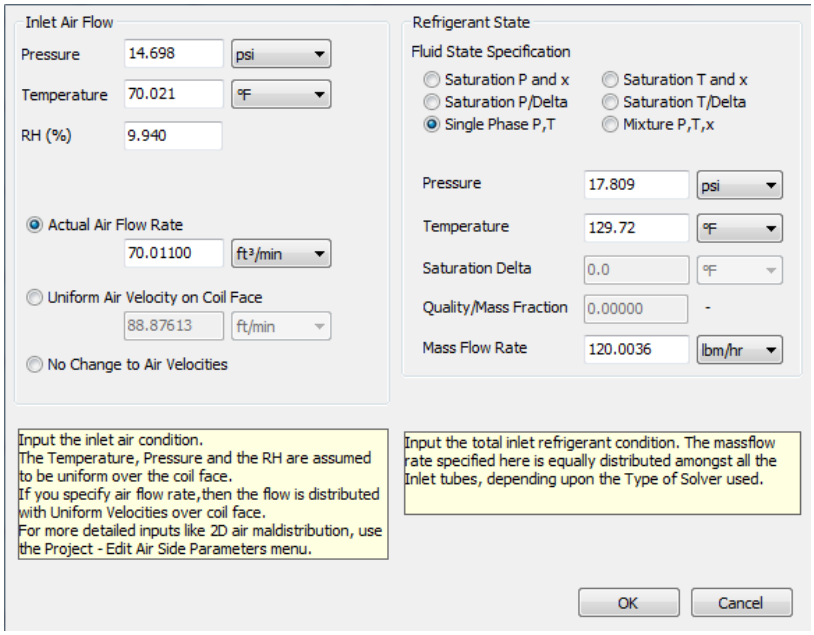

Figure 2.5: Example of inlet conditions input page from CoilDesigner™

Once inlet conditions are set the simulation is ready to run. CoilDesigner™ runs through the analysis and outputs a significant amount of data that can be used to detail the performance of the MCHX or serve as checks for some of the intermediate calculations done in the software. The main results used for this study are the total heat load and refrigerant and air outlet temperatures. Other output results for charge amount, air and refrigerant pressure drop as well as primary and secondary areas and heat transfer coefficients are calculated during the analysis.

2.4.2 COILDESIGNER™ VALIDATION

When developing the MCHX tool in CoilDesigner™ a significant study was done to validate the results from the modeling software. Huang et al. (2014a) validated CoilDesigner™ to 227 data points using 18 different geometries and eight working fluids. Heat capacity predictions were correlated within 2.7% on average.

The procedure outlined by Huang et al. uses the overall heat transfer coefficient method using the arithmetic mean temperature difference instead of the log mean temperature difference commonly used for heat exchanger analysis. The arithmetic method was shown to have a negligible effect on the results but proved to be faster and more robust than the log method. There is little effect because of the discretization method used, so the small segments yield very smilar results using the two methods. Each tube is broken into a number of segments defined by the user and each segment is stepped through to get to the outlet. Before Huang et al., MCHX modeling software was limited to uniform geometries and inlet conditions. This was accomplished by calculating heat transfer coefficients at the port level and solving for the top and bottom of the port individually. The control volume extended through the center of the fin on either side of the port. A port is another name for an individual channel in the microchannel tube. Using this model each control volume contains one refrigerant flow and two independent airflows.

Huang et al. also outlined the correlations used for the different geometries and fluid states during validations. For single-phase refrigerant side heat transfer the Gnielinski (1979) correlation was used and the results were favorable. Gnielinski will be used for the present study as well. Since water is the working fluid two-phase flow correlations won't be required. Huang et al. also used the Chang and Wang correlation described in Section 2.3 for the louver fin; their results validate the selection of this correlation for the present study.

2.5 Scope of Work

The scope of the present work is to investigate the maldistributed airflow around a microchannel condenser. The maldistribution will be generated by experimenting with uniquely shaped heat exchangers. The goal is to connect the shape and maldistributed airflow to the effect it has on the overall performance of the heat exchanger.

Specifically, three geometries will be looked at: a flat MCHX as a baseline, a U-shape, and a roll shape. HX airflow rates in the range of 40-100 CFM will be considered throughout this study and translate to local velocities from 35-180 FPM depending on geometry and measurement location. Each condenser shape will be tested inside a water calorimeter to measure the performance of each coil. The local velocity profile will be measured using an appropriate technique for each coil in this study. Two types of anemometer as well as a particle image velocimetry technique were used to improve the measurement resolution. The measured local velocity profile will be applied in the heat exchanger modeling tool CoilDesigner™ to compare the model predictions of heat capacity with the experimental results from the water calorimeter. The results will help to quantify the effect of maldistributed airflow on MCHX thermal performance. The effect of the uniform airflow assumption will also be directly compared to the measured maldistributed profile effect on the modelling result independent of the calorimeter result.

3 HEAT EXCHANGER CONSTRUCTION

During this study three heat exchanger shapes were considered. Each has a similar construction as it pertains to materials used and processing, but may differ in size and internal geometry between the shapes. There are also some variables and terminology to be familiar with when looking at MCHXs.

MCHXs get their name from the microchannel tubes the refrigerant flows through. Figure 3.1 shows a cross section of a microchannel tube. The small channels or ports in the tube increase the surface area to volume ratio between refrigerant and the tube, and the tube and air. Louvered fin material is commonly paired with a microchannel tube design. The fins are folded accordion style along the length of the fin. The fins are placed between the tubes and the fin length is oriented in the direction of airflow. The two consequences to this fin orientation are the louvers protrude into the airflow and airside pressure drop is lower than having the fins aligned in the other direction. An image displaying standard louver fin geometry and cross section is shown in Figure 3.2.

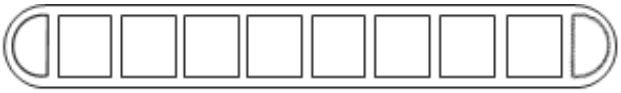

Figure 3.1: Cross-section of a microchannel tube

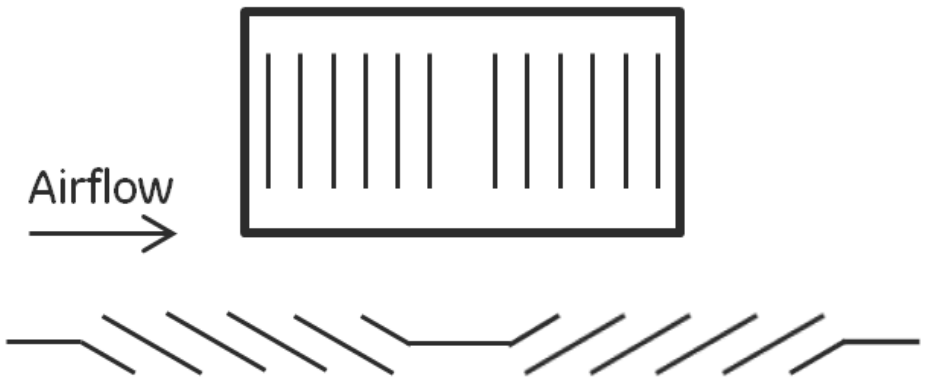

Figure 3.2: Top view (top) and cross-section view (bottom) of louver fin geometry

3.1 MCHX Circuiting

MCHXs have many tubes that run in parallel. A common method of construction is to bank some of the tubes together to provide multiple passes using a manifold. As an example, the flat MCHX used in this study is shown in Figure 3.3. This is called a two pass MCHX because the refrigerant travels down through 11 tubes and back through 3 tubes as shown by the arrows. The black line across the left header shows where the baffle is that separates the two banks of tubes.

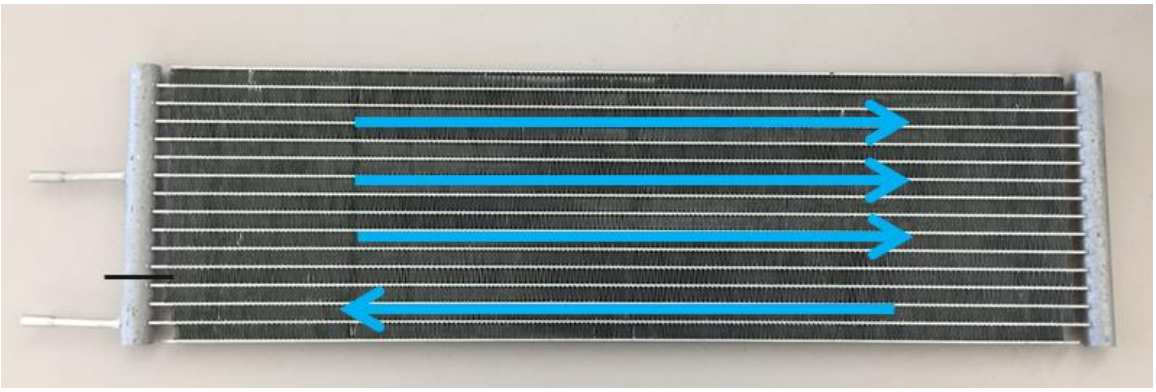

Figure 3.3: Circuiting for two pass flat MCHX

Many studies have been done to determine what circuiting technique is the best for the capacity of the coil. When the coil is used as a condenser the refrigerant enters as a vapor and exits as a liquid. Looking at Figure 3.3 it would make sense that the inlet would be the top portion with 11 tubes to hold the high volume vapor and the bottom portion would be for the outlet lower volume liquid phase. Using multiple passes increases the capacity of the coil but the additional heat transfer per pass decreases as the number of passes increases. This was clearly shown in a study done by Subramaniam and Garimella (2005) where they conducted a parametric analysis on many geometric characteristics for a MCHX. Their goal was to optimize the mass of the MCHX while maintaining the baseline heat duty of a condenser. They were able to show that the pass arrangement had the greatest effect on performance optimization. This was taken a step further by Mehendale et al. (2014) when it was shown that a contracting tube distribution for each pass was shown to optimize the heat duty of a given condenser arrangement.

3.2 MCHX Shapes

The first shape used in this study was a flat MCHX shown in Figure 3.4. The flat MCHX is the easiest shape to study because there should be no airflow maldistribution. This is also the shape of the most notable MCHX application in industry today, the car radiator. Using the flat shape as a baseline it can be understood how accurate the analysis of the other shapes could hope to be when comparing the predictions from the correlations and the experimental results.

Figure 3.4: Flat MCHX sample

The airflow path through the flat MCHX is shown in Figure 3.5. The airflow across the face of the MCHX is expected to be uniform; top to bottom and side to side. The fan is shown on the right that is drawing air through the coil. The schematic shows the MCHX in open air but in practice this isn't the case. The MCHX has ducting around it to connect one side to the fan source; the other side is open to the air.

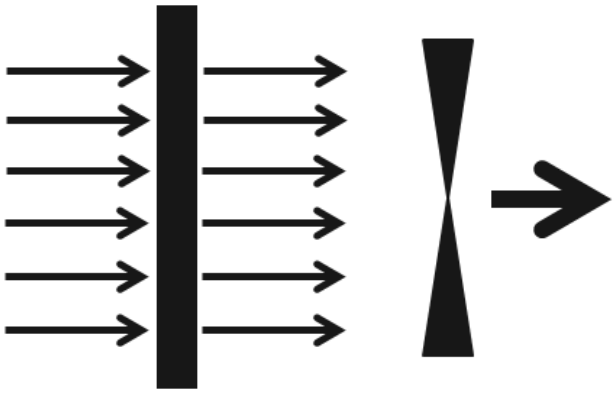

Figure 3.5: Side view of the uniform airflow path through the flat MCHX

The second sample considered in this study is a U-shaped MCHX, shown in Figure 3.6. The U-shape will present the first example of maldistributed airflow along the face of the HX. The construction of the U-shape sample differs from the flat in more than just shape.

The U-shape has an extra tube, is four pass (5-4-3-3) and the header length increased because of the extra tube. This means the U-shape has a greater internal volume than the flat and has a slightly higher potential for heat capacity than the flat. The shape may keep it from having a higher heat capacity because of the maldistributed airflow. The other geometric parameters for the U-shape are the same as the flat.

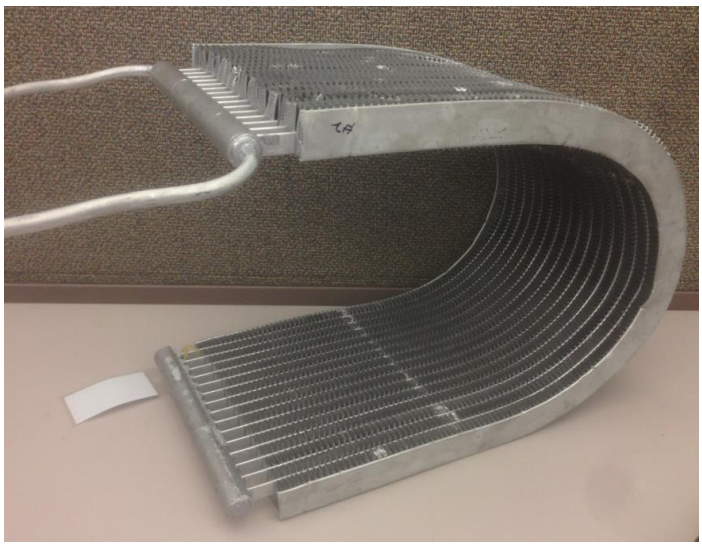

Figure 3.6: U-shaped MCHX sample

A schematic for the U-shape airflow is shown in Figure 3.7. The airflow around the U-shaped MCHX is expected to change along the length of the tubes as the distance from the fan increases or decreases. Sections of the heat exchanger further from fan may be expected to have lower flows. The air is drawn through the fins and exits out the middle. The open top and bottom of the U-shape are sealed so that air can only be pulled through the fins and exit out the open end where the fan is shown in the schematic.

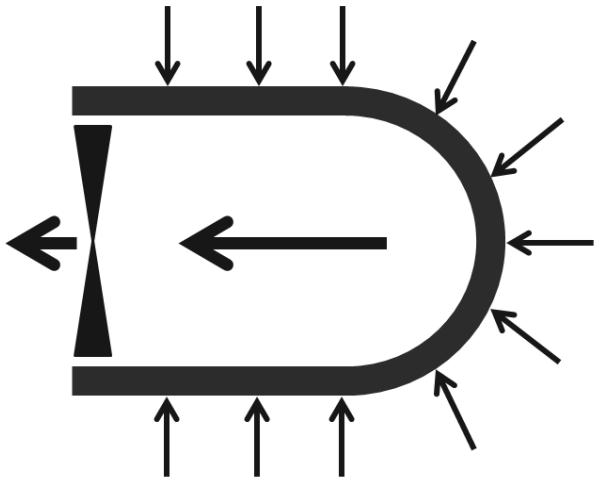

Figure 3.7: Top view of airflow path around U-shaped MCHX

The third sample in this study is the roll MCHX, shown in Figure 3.8. The roll shape is a unique geometry that should have an interesting air velocity profile. The construction of the roll MCHX is the exact same as the flat MCHX just formed into the roll shape. This is expected to be the best comparison in this study for the effects of maldistribution because of the apples to apples comparison with the flat performance.

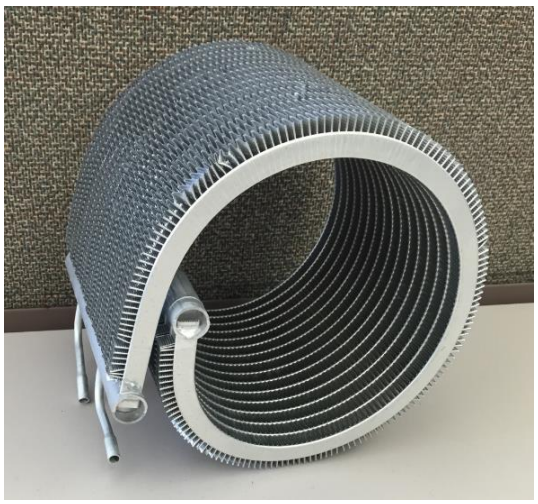

Figure 3.8: Roll MCHX sample

Figure 3.9 shows the airflow through the roll MCHX. The images show the front (L) and side (R) views of the roll MCHX with the fan drawing air radially through the fins then exiting axially. On one end of the roll is the fan, the other end will be capped to block airflow and force air across the fins and tubes.The velocity is expected to decrease as axial distance from the fan increases, which means each tube would have a different local velocity.

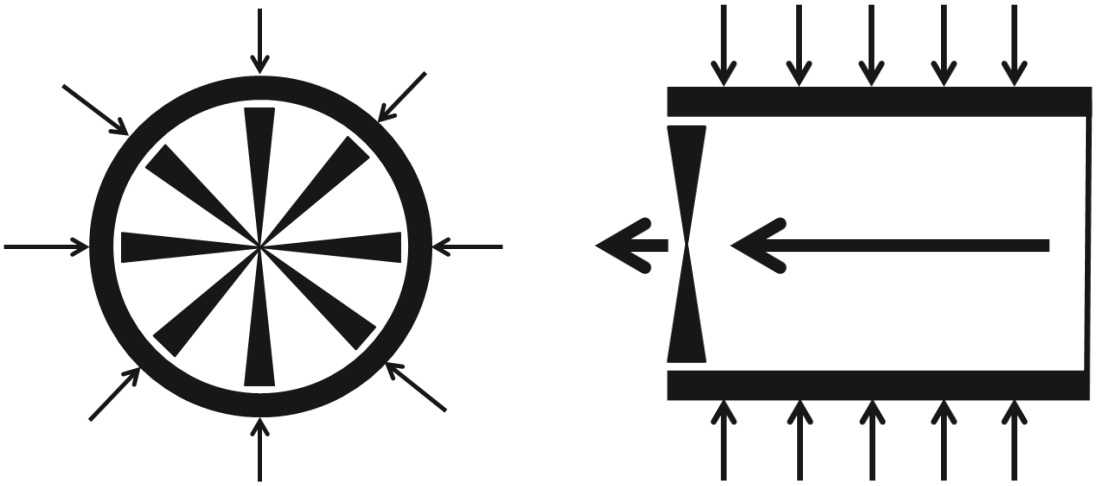

Figure 3.9: Airflow through the roll MCHX; front (L) and side (R) views

3.3 MCHX Area Density

As described in Section 2.2, heat exchangers can be classified based on surface area density. As long as either the air side or refrigerant side area densities meet the criteria the HX can be considered compact for that particular application. The area densities for the MCHXs for this study are shown in Table 3.1. The results show for either

construction the classification is compact since a liquid, two- phase HX is required to have an area density above 122 ft^2/ft^3.

Table 3.1: Area Densities for flat, roll and U-shaped MCHXs

MCHX Shape	Refrigerant Side			Air Side		
	A (ft^2)	∀ (ft^3)	A/∀ (ft^2/ft^3)	A (ft^2)	∀ (ft^3)	A/∀ (ft^2/ft^3)
Flat/Roll	2.84	0.0045	624	16.46	0.0258	637
U-shape	3.46	0.0046	750	23.59	0.0356	663

The two geometries are quite comparable when it comes to air-side area density. The U-shape has a larger surface area on the refrigerant side but almost identical volume compared to the flat/roll. This is due to the U-shape having smaller ports but one more tube and tubes that are approximately 5" longer than the flat/roll construction.

4 TESTING APPARATUS

4.1 Water Calorimeter

The heat exchangers being studied were tested in a water calorimeter. The condenser is a refrigerant-to-air heat exchanger and has two fluids to consider. The working fluid is typically a refrigerant but is replaced with water to make the calorimeter calculations more accurate as the water will remain liquid. Using a common refrigerant would add complications and uncertainty because a phase change would occur and the correlations required are less accurate. Figure 4.1 shows the water calorimeter setup with the roll microchannel heat exchanger installed. Shown at the right of the picture are four RTD (resistance temperature detector) sensors that measure the air inlet temperature. The copper tubes shown in the background deliver water to the heat exchanger. On the other side of the heat exchanger are more RTDs to measure the outlet air temperature. The liquid temperatures are measured in the process lines that are connected to the copper tubes out of the picture.

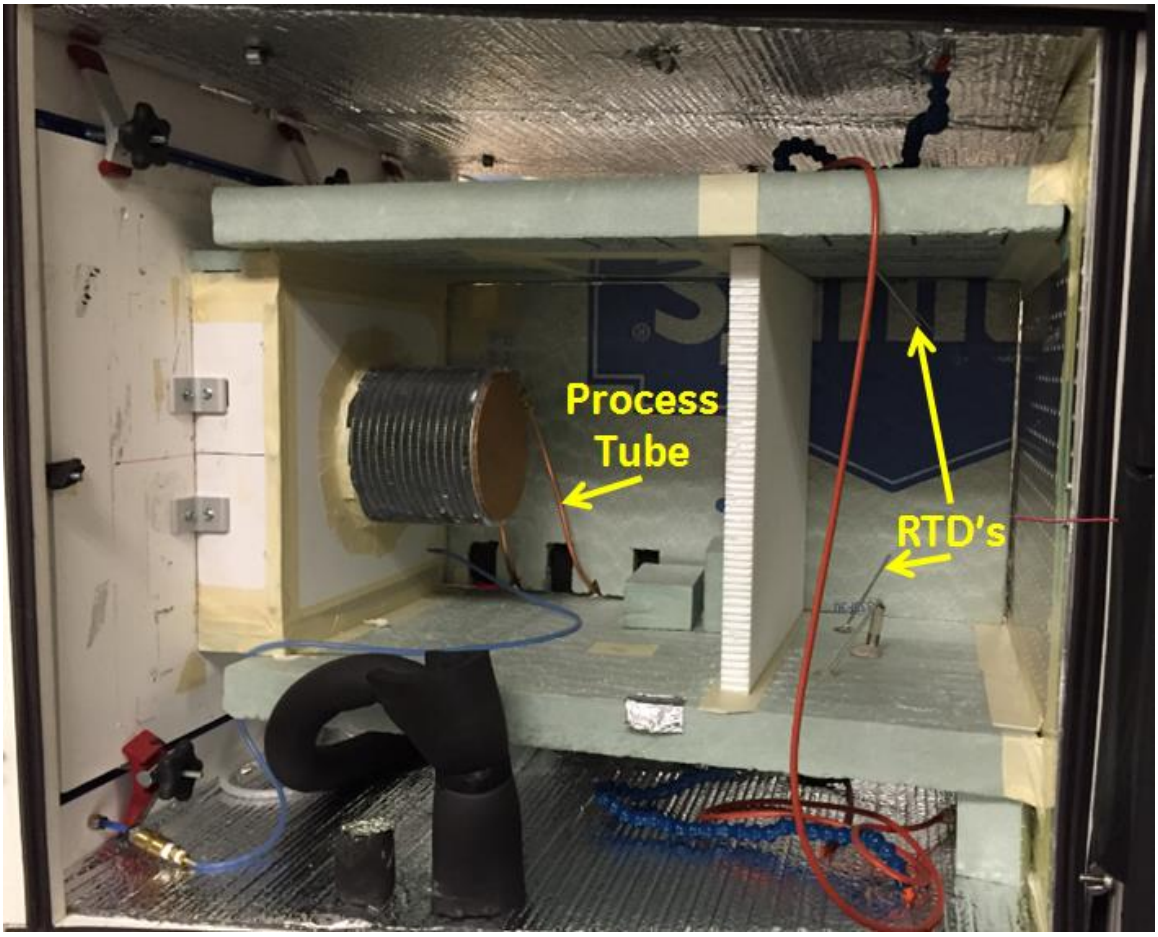

Figure 4.1: Water calorimeter with rolled microchannel condenser installed

By measuring the air and liquid temperatures, as well as the flow rates for both, we can calculate the heat energy in each medium. Theoretically all of the heat removed from the liquid should be transferred to the air. Of course this isn't the case experimentally because of small unavoidable heat losses at different points in the process. Figure 4.1 show three sides of the foam box that constrains the flow around the heat exchanger. This box is sealed and the air temperatures in that box can be thought of as the inlet conditions seen by the heat exchanger. Air is being drawn through the HX and exits through the open end into the left wall of the picture.

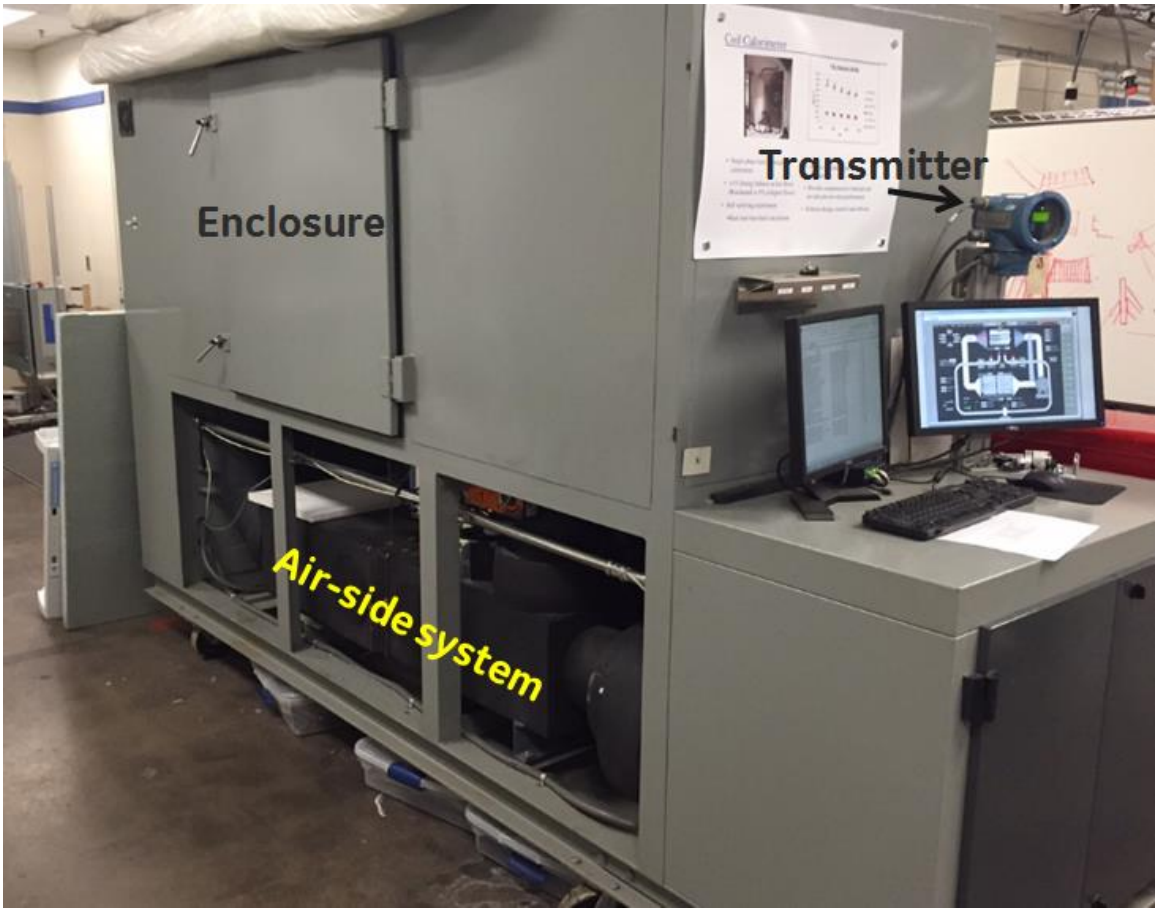

Figure 4.2: External view of the water calorimeter

There is another enclosure outside of the foam box in Figure 4.1 and all of that sits inside the large enclosure shown in Figure 4.2. The free spaces between the enclosures are filled with blanket insulation to further reduce heat loss. Also shown at the bottom of Figure 4.2 is the air-side system of the calorimeter. In simple terms it is an insulation wrapped wind tunnel outfitted with heaters and blowers to provide the proper inlet air conditions required to test different heat exchangers. Behind the air-side system is the liquid-side system with the appropriate pumps, heaters and valves necessary to produce the inlet liquid conditions. On the right of Figure 4.2, above the computer monitor, the mass flow

meter transmitter for the liquid is shown. The actual mass flow meter is hidden beneath the calorimeter. The mass flow meter is a Micro Motion Elite Coriolis Flow and Density Meter.

Calorimeter tests are run using a random order of the specified inlet test conditions. Typically a matrix of tests is done; one for each airflow rate at each liquid mass flow rate. When a new set point is given the system has a set amount of time to stabilize. If in that given amount of time, three hours for these tests, the system cannot stabilize it will move onto the next point in the series. The stabilization criterion for these tests was an inlet air temperature of 70 ± 2°F and an inlet liquid temperature of 130± 1°F. There are various reasons the system would fail to stabilize. Often the airside has a difficult time stabilizing due to the stratification of flows at lower airflow rates. This causes the four inlet RTDs to have different readings and fail the stability criteria for airside inlet temperature.

4.2 Wind Tunnel

The wind tunnel served two purposes during the study of different MCHX shapes. First, the wind tunnel allowed precise control over the total flow rate through the HX so that local velocities across the face of the HX could be measured. The wind tunnel consists of a tunnel, blower and differential pressure gauges to calculate the flowrate and measure pressure drop. Figure 4.3 shows the flat MCHX installed and the blower on the bottom of the wind tunnel cart. There are a few differential pressure sensors available depending on the flow rates used in the study. The program that runs the wind tunnel was made using

LabVIEW™. The wind tunnel used in this study is a 500 CFM chamber that is 48” long and has a diameter of 16”.

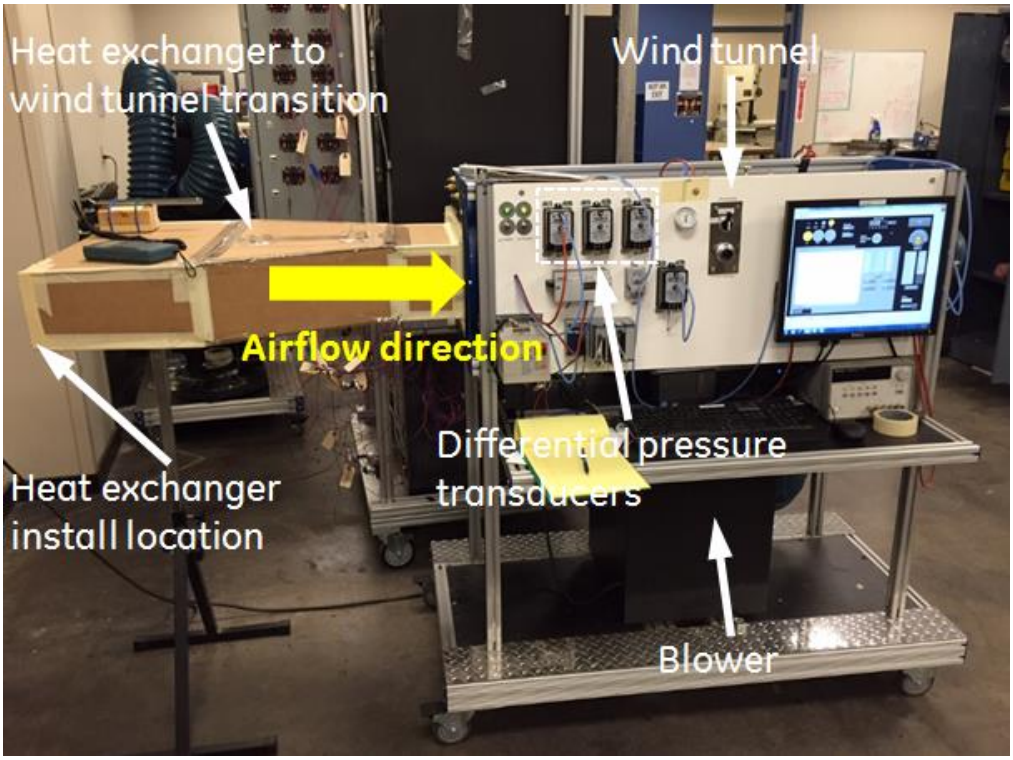

Figure 4.3: Flat MCHX installed on the wind tunnel for local velocity measurements. Note: airflow is left to right as it is drawn into the tunnel

The pressure transducers used on the wind tunnel come from Setra Systems© and are shown in Figure 4.4. When measuring flowrate through the wind tunnel the process lines are connected to the pressure transducers that are on either side of the nozzle plate and controls how much flow is moving through the system. Flow rate through the wind tunnel is precisely measured by opening the nozzles necessary for the corresponding flowrate range and selecting the appropriate transducer to measure the pressure drop across the nozzle plate. The LabVIEW™ software that operates the wind tunnel does the conversion from pressure drop to flowrate after the user inputs which nozzles are open using a well-

defined algorithm for this wind tunnel. When measuring pressure drop, as air is drawn through the HX (not blown through), the high pressure side will be the ambient and the low pressure side will be inside the wind tunnel. No tubing is connected to the high side of the transducer and the low side will be connected to the pressure port just after the heat exchanger.

Figure 4.4: Setra Systems© differential pressure transducers used to measure pressure drop on the wind tunnel with ranges of 0-5" WC, 0-2.5" WC and 0-0.1" WC

The second purpose of wind tunnel was pressure drop testing. As will be described in the next section, painting the HX flat black is necessary for PIV (Particle Image Velocimetry) which is another method of measuring local air velocity. Pressure drop curves were needed to ensure there was little effect in the airflow by adding a paint layer. Figure 4.5 shows images of the rolled MCHX installed on the wind tunnel pre and post paint.

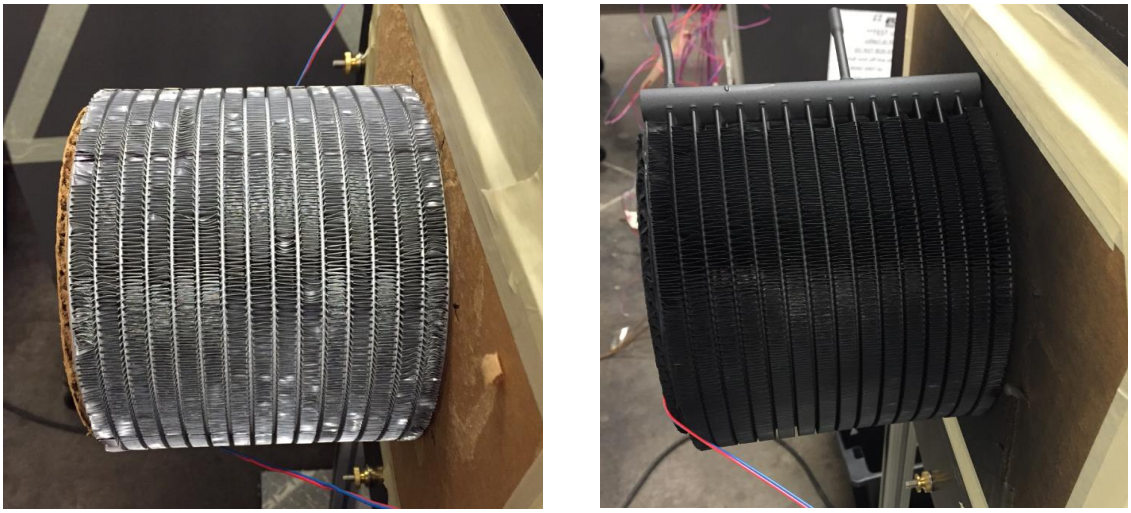

Figure 4.5: Not painted (L) and painted (R) samples of MCHXs for pressure drop testing prior to PIV analysis

For the pressure drop tests the 0.1”H_2O sensor shown on the right of Figure 4.4 was used. The results of the pressure drop test are shown in Figure 4.6. The curves lay right on top of each other so the paint seems to have a negligible effect on the airflow of the condenser. This means the PIV data should accurately represent the flow for an unpainted sample.

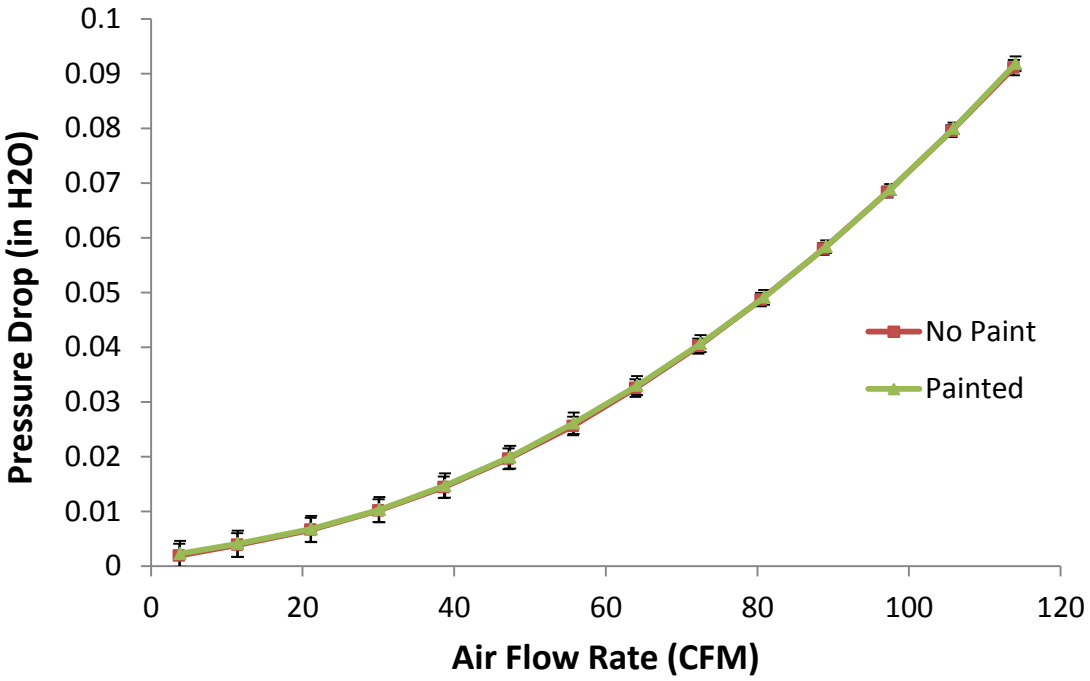

Figure 4.6: Pressure drop curves show no significant change in airflow when the roll MCHX has been painted

4.3 Velocity Measurements

It is difficult to accurately measure local velocities with much precision on compact heat exchangers. The things that can make this difficult are curved surfaces, invasive measurement techniques, sensor measurement range and resolution and the size of the instrument effectively averaging results over a large area. Multiple techniques were utilized to increase confidence in the results.

4.3.1 VANE ANEMOMETER

The vane anemometer used as one of the measuring devices can also be seen in Figure 4.7. The AV6 vane anemometer is a 100 mm diameter anemometer that can measure air

speed in the range of 50-6000 ft/min. With the sensor that large, it is expected that these results will serve only as an estimate of the flow profile across the face of all three geometries being studied in this paper. The method of averaging and defining the velocity is discussed in Section 5.2.

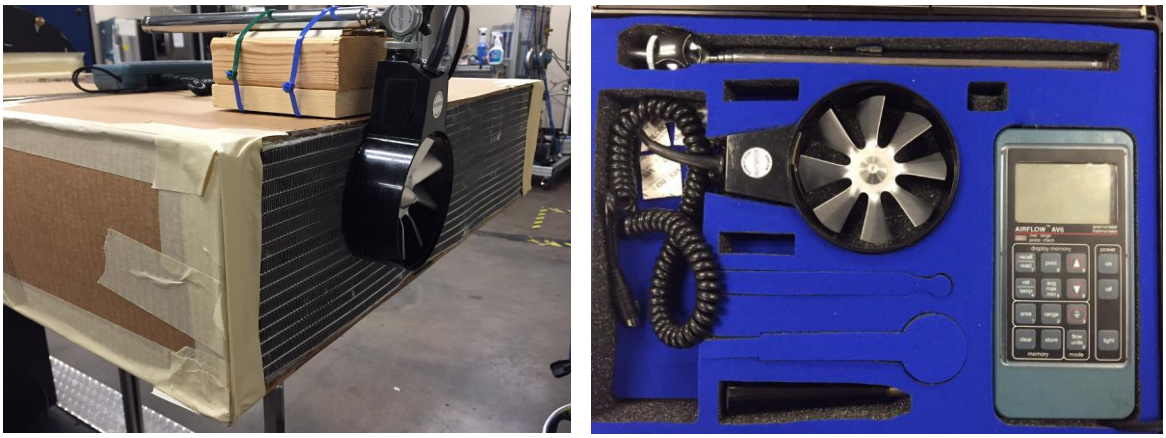

Figure 4.7: Airflow AV6™ digital handheld vane anemometer (R) shown measuring local velocity on a flat MCHX (L)

4.3.2 PIV

Particle image velocimetry or PIV is different from typical methods of analyzing airflow because it is a non-invasive measurement technique. Using an anemometer with the wind tunnel, for instance, disturbs the airflow and the results are for this modified flow. In PIV testing, particles used to see the flow are tuned such that the particles don't have any buoyancy effects or affect the flow. The PIV setup used in this experiment is shown in Figure 4.8. The idea behind PIV is to follow particles as they move during very short time periods and calculate their speed based on distance travelled over the time interval. This is done using a laser curtain and two cameras that capture the particle image in the

laser curtain. The background and HX need to be black in order for the camera to be able to see the particles. With the cameras pointed at an angle, measurements of particle position in X, Y and Z coordinates can be obtained.

Figure 4.8: PIV setup for roll MCHX (Add arrows and labels)

The process works by analyzing side by side pictures of the flow with the left and right cameras as shown in Figure 4.9. Approximately 100 microseconds after the first, another set of images is taken and the post processing software is able to calculate the speed of the particles. The result is a grid of three dimensional velocity vectors. Fifteen sets of data for a given flow field are averaged to produce a color map of the velocity field. An example of one of these color maps is shown in Figure 4.11. Most of the data is around the top of the HX because during the PIV setup the software has to be told an area to concentrate on and masks the rest of the background. The laser cannot pass through the

HX so the vector grid and corresponding color map are limited to areas near the top of the HX and only partly down one side.

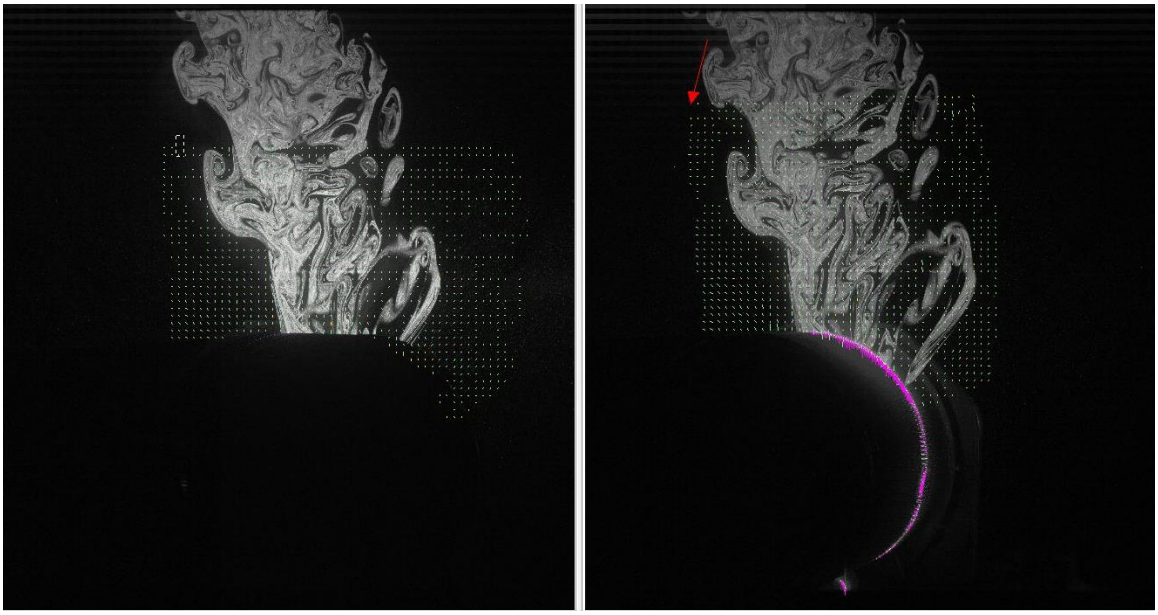

Figure 4.9: Images taken by the PIV cameras

A big plume such as shown in Figure 4.9 is not of concern to the process and is a result of the method of infusing particles into the air. The plume indicates an area where there are many particles but that shouldn't affect the result. The important aspect of the image is the vector grid; Figure 4.10 has a zoomed in image of part of the vector grid. The vector lengths are based on magnitude so the highest speed locations have longer vectors. The faint white specs amongst the black space are the particles used for the PIV measurements.

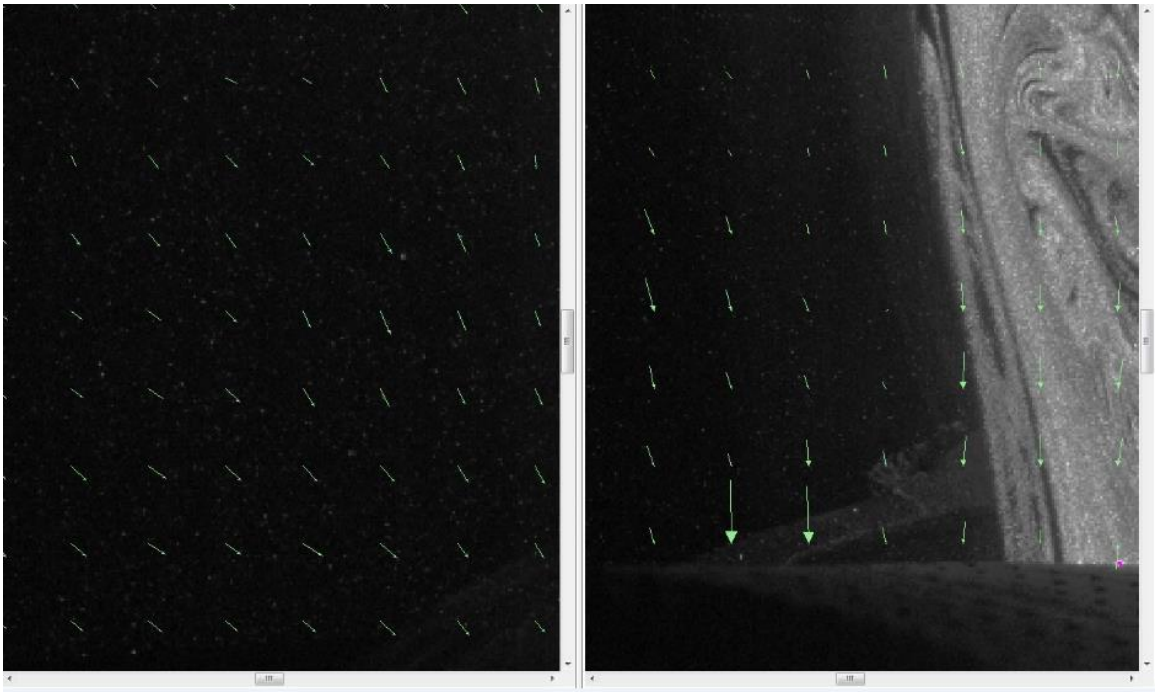

Figure 4.10: Zoomed in image of pictures taken by PIV cameras

The PIV system used in this study is a 3D Stereoscopic PIV system made by TSI Inc. The software used to analyze the images was Insight 4G™. This experiment setup used a 1mm thick laser sheet and particles 3-5μm in diameter. The particles are sized such that buoyancy effects are negligible. An important measurement for this type of study is to make sure the particle count per quadrant is high enough. The software that analyzes the image can count the particles so the particle count is kept high enough to get a good result. The TSI manual follows rules of thumb developed by Keane and Adrian (1990) for PIV analysis. For instance, the rule of thumb for particle count is ten particles per quadrant. For the particle to count it must be in the same quadrant for both images. Other rules of thumb pertain to the range of acceptable displacements between the images as they relate to the quadrant size, particle size and laser sheet thickness.

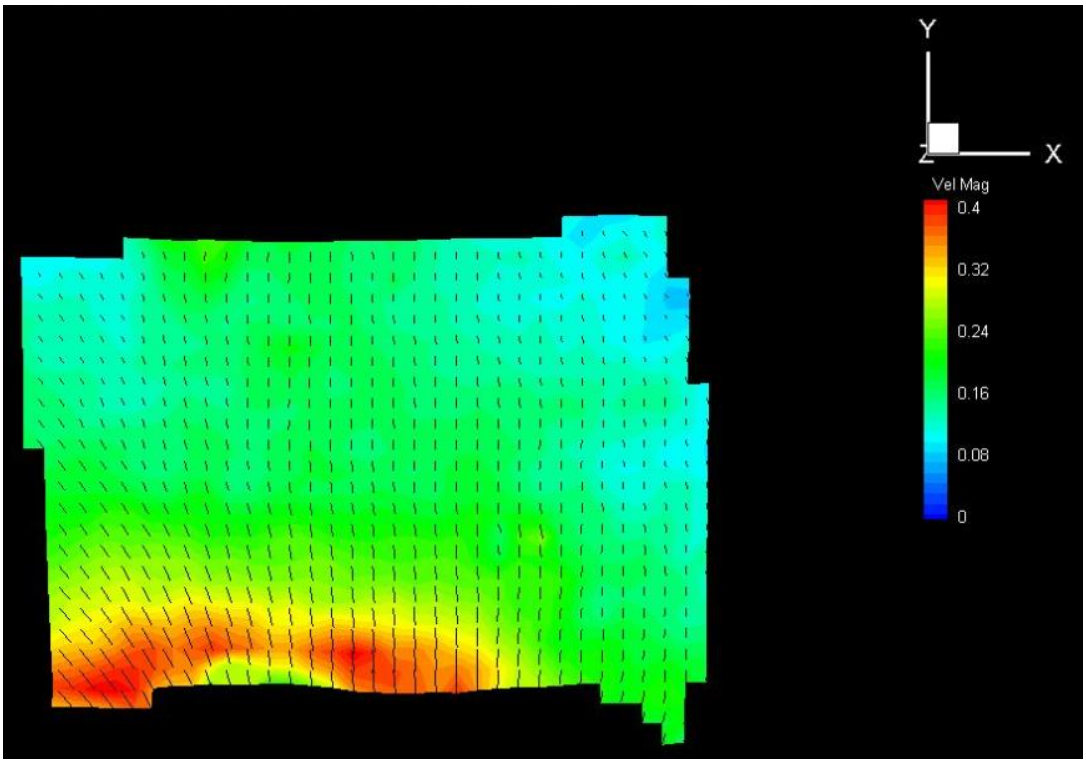

Figure 4.11: Example of PIV results for velocity magnitude for area above rolled MCHX

4.3.3 HOT WIRE ANEMOMETER

To have something to directly compare with the PIV results the twelve o'clock position on the roll MCHX was measured using a hot wire anemometer. At low airflow rates the vane anemometer is disadvantaged because a larger vane is required to be able to measure low speeds. The hotwire anemometer has a small diameter so more resolution can be achieved using a hotwire. The diameter of the hotwire probe is 3/8" compared to the almost 4" diameter vane anemometer. The downside to the hotwire is it is more sensitive to orientation and placement because the footprint is so much smaller than the

vane anemometer. The hotwire anemometer used in this study is the Graywolf AS-201 sensor shown in Figure 4.12.

Figure 4.12: Graywolf AS-201 hotwire anemometer used to measure local airflow rates

Hotwire anemometer measurements were taken using the same setup as the PIV measurements shown in Figure 4.8. A fan was installed on the open end of the roll MCHX and measurements were taken with the anemometer along the twelve o'clock position. The probe was positioned such that the sensor opening was aligned flat on the HX surface to minimize orientation errors. Graywolf provides a software program called WolfSense 2015 that displays the results and allows test duration and time between samples to be set. Ten samples were taken for each measurement location over a 30 second duration.

4.4 Test Uncertainty

With many different sensors recording information that will be used to calculate important performance characteristics of HX performance it is important to outline the uncertainties from those measurements and how they will propagate into the calculated values. In general the method will be to combine accuracy, precision and resolution uncertainty for each measurement using Equation [4-1]. In most cases, the accuracy error will be stated by the equipment documentation, the resolution error will be half of the resolution of the measurement device, and the precision error will be two times the standard deviation of the repeated data points. The measurement uncertainty will be carried through calculations using the partial derivative method presented by Holman (2001) and is shown in Equation [4-2], where a, b, c are measured quantities and X is the calculated quantity.

$$\delta a = \sqrt{\delta a_{accuracy}{}^2 + \delta a_{precision}{}^2 + \delta a_{resolution}{}^2} \quad \textbf{[4-1]}$$

$$\delta X = \sqrt{\left(\frac{\partial X}{\partial a}\delta a\right)^2 + \left(\frac{\partial X}{\partial b}\delta b\right)^2 + \left(\frac{\partial X}{\partial c}\delta c\right)^2} \quad \textbf{[4-2]}$$

4.4.1 WATER CALORIMETER UNCERTAINTY

The high precision RTDs used in the water calorimeter come from Omega Engineering© and are “Class 1/10Din.” The accuracy specification for this class of sensor is ±1/10(0.3 + 0.005|T|) °C. This translates to 0.08°C or 0.14°F of accuracy error at the highest temperature these sensors can measure. On the air side there are four inlet RTDs and

eight outlet RTDs. On the liquid side there are two inlets and two outlet RTDs. Having multiple RTDs will allow precision uncertainty calculations to be made. The stated accuracy for mass flow is ± 0.10% of measured rate. According to the performance specifications the accuracy uncertainty includes a ± 0.05% repeatability uncertainty. For calorimeter tests that means a maximum combined accuracy and precision uncertainty of $0.14 lb_m/hr$ for a $140 lb_m/hr$ operating point. By combining Equations [4-1] and [4-2] the total uncertainty for the liquid side heat capacity can be derived. Since the specific heat of water, c_p, is a very well known quantity we are assuming there is no uncertainty in that value. The error propagation result for the rate of heat transfer for the liquid is shown in Equation [4-3].

$$\delta_{q_{liq}} = \sqrt{\left(c_p(T_o - T_i)\delta_{\dot{m}}\right)^2 + \left(\dot{m}c_p\delta_{T_o}\right)^2 + \left(\dot{m}c_p\delta_{T_i}\right)^2} \qquad \textbf{[4-3]}$$

4.4.2 WIND TUNNEL UNCERTAINTY

The differential pressure transducers all have an accuracy of ±1% FS at constant temperature. Since the accuracy is based on full scale range it is best to use the sensor that fits closest to your test setup and not just the one with the largest range. During the pressure drop test two sets of data were taken using sensors with a 0-0.1 inH_2O range and 0-1 inH_2O range. The precision error resulting from the two measurements was small because the sensors measured very close to each other and the accuracy error accounts for 0.001 inH_2O using the $0.1 inH_2O$ sensor.

4.4.3 ANEMOMETER UNCERTAINTIES

The AV6 anemometer shown in Figure 4.7 has an accuracy of ±1% of the reading at room temperature. The resolution of the anemometer is 2 fpm so the resolution uncertainty is 1fpm. The measurements taken with the AV6 oscillated significantly so the precision error was quite high, accounting for more than 90% of the total uncertainty.

The hotwire anemometer shown in Figure 4.12 has an accuracy of ±3% of the reading ±3 fpm and a resolution uncertainty of 0.5 fpm. The precision error calculated from the standard deviation from taking multiple data points was the highest source of uncertainty in the hotwire anemometer testing.

5 EXPERIMENTAL RESULTS

The most important performance characteristic of a heat exchanger is the heat capacity. The MCHXs were tested inside a water calorimeter to measure outlet temperatures and heat capacity while varying water mass flow rate and airflow rate. The heat capacity and temperatures from the calorimeter will be compared to the prediction results from the modeling software.

The MCHXs tested were also put on a wind tunnel where local air velocity could be measured. Using local velocity the airflow distribution could be quantified and applied to the simulation model to see if the simulation results would approach the experimental results measured from the calorimeter. The model was then further manipulated to see the effect of increasing levels of airflow maldistribution. PIV (particle image velocimetry) was also used to analyze one of the coils. The purpose of PIV was to corroborate or refute the other methods of airflow measurement using a non-intrusive technique.

5.1 Heat Transfer Capacity

The heat transfer capacity or heat transfer rate, q, is a key design parameter and performance indicator for a heat exchanger. As it pertains to system design, the capacity of a coil is its ability to exchange enough heat to achieve the desired operating conditions.

For the sake of this study, where the MCHX is used as a condenser, the heat transfer capacity of the MCHX would limit the amount of heat the system can reject.

In order to experimentally determine q for a given coil, the temperature of the fluid entering and leaving the heat exchanger and the mass flow rate of the fluid must be measureable. This is where the water calorimeter, described in Section 4.1, will be used. During calorimeter testing the inlet and outlet temperatures and mass flow rates for the air and the water are measured. Using this data the heat capacity of the HX can be calculated. The calculation for heat capacity q, for the single phase liquid side, is shown in Equation [5-1].

$$q_{liq} = \dot{m} c_p \Delta T_{liq} \quad \textbf{[5-1]}$$

The calculation for heat capacity is straight forward for the liquid side because the water calorimeter is outfitted with a mass flow meter. The calculation is less so for the air side as a volume flow rate and air density are used to determine mass flow rate, as shown in Equation [5-2]. The air density was calculated using known values of barometric pressure and temperature.

$$q_{air} = \dot{\forall} \rho c_p \Delta T_{air} \quad \textbf{[5-2]}$$

In a perfect system all of the energy that leaves the warmer liquid, q_{liq}, would be found in the air, q_{air}. The difference between these two quantities is a measure of the energy balance of a given test and it is expressed as a percent. The rule of thumb used when operating the water calorimeter is have no more than 3% difference between the air and liquid heat capacities. When doing analysis on the performance of the coil it is best to use

the liquid side temperatures and heat capacities because the measurements are more stable than those on the air side because they are less affected by the surroundings.

5.1.1 FLAT

The Chang Wang louver fin correlation, described in Section 2.3, is meant to be used on a flat heat exchanger geometry where the direction of flow is perpendicular to the fins and the heat exchanger face is in one plane. Since the aim of this study is to look at the effect of different shapes it is important to validate the correlation and experimental setup with data obtained for the precise situation the correlation was designed to handle.

To start, two runs were done with the flat MCHX on the calorimeter, shown in Figure 5.1. The first test, shown in the image on the left, had an average energy balance of 4.2%. This means 4.2% of the heat was being lost to the surroundings due to difficulties insulating the water calorimeter effectively. The flat MCHX setup pushed the limits of the water calorimeter because of its size. The flat was almost too big to fit inside the envelope dimensions of the calorimeter and some of the insulation typically installed had to be removed. A second attempt is shown on the right of Figure 5.1. In the second setup the coil was completely enclosed and the ambient volume made much smaller. The energy balance was improved but only to 4%. This is not ideal but further improvement would be hard to come by.

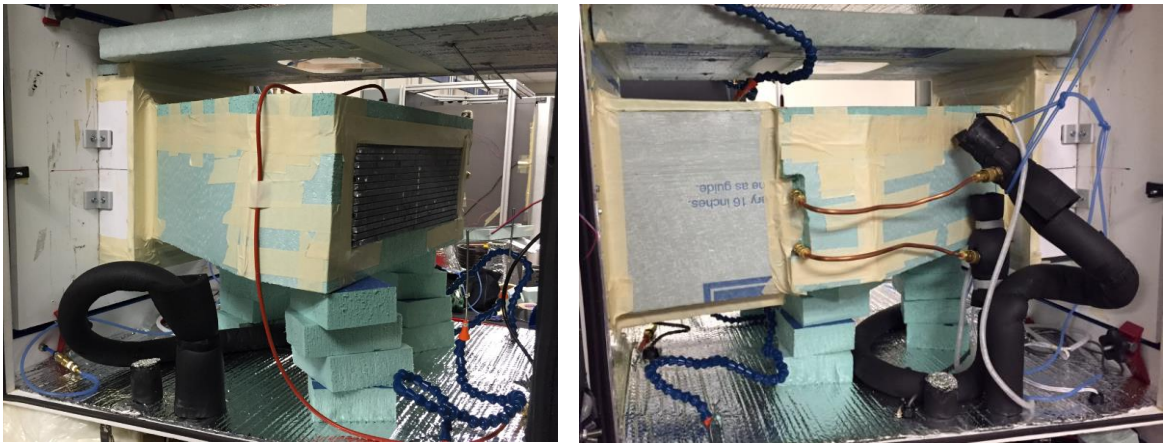

Figure 5.1: Flat MCHX installed in water calorimeter before (L) and after (R) setup modifications for energy balance improvements

The water calorimeter input conditions were set such that the air and liquid inlet conditions remained constant at 70°F and 130°F respectively for every test. The variable conditions were airflow rate and liquid mass flow rate. The resulting dependent quantities of interest were outlet temperatures, energy balance, and heat capacity.

Table 5.1 shows the results of the calorimeter testing with the flat MCHX installed. The obvious trends are the increase in heat capacity as airflow rate (40-70 CFM) and liquid mass flow rate (120-140 lb_m/hr) increase. The difference in energy balance for the whole data set averaged to 4% but the instability is largely due to the lower airflow rate set points. Within a given airflow rate and varying liquid mass flow rates the difference in energy balance changes by at most 0.7% whereas the difference in energy balance changes by 3.3% at most for a given liquid mass flow rate and varying airflow rate, indicating that airflow rate is the main contributor to a higher difference in energy balance. The 50 CFM/120 lb_m/hr data point is missing from this set because it didn't reach stable inlet conditions.

Table 5.1: Heat capacity of flat MCHX from water calorimeter testing

Airflow Rate (CFM)	Liq Mass Flow Rate (lb_m/hr)	ΔT_{liq} (°F)	Difference in Energy Balance (%)	Q_{liq} (BTU/hr)
40	120	14.4	5.4	1906
40	125	18.4	6.0	1933
40	130	20.5	5.5	1930
40	135	19.9	5.3	1941
40	140	24.3	6.0	1969
50	125	15.9	4.3	2297
50	130	17.2	4.1	2318
50	135	21.8	3.8	2313
50	140	22.9	4.3	2339
60	120	15.5	3.3	2613
60	125	17.9	3.3	2635
60	130	16.7	3.5	2664
60	135	23.5	3.3	2680
60	140	22.3	3.6	2697
70	120	14.1	3.1	2913
70	125	14.9	2.7	2938
70	130	21.1	2.8	2969
70	135	19.3	2.9	3005
70	140	21.7	3.0	3034

5.1.2 U-SHAPE

The U-shape MCHX is of a different construction than the flat sample used as the baseline. The number of tubes and envelope dimensions are different than the flat sample. The U-shaped MCHX is shown installed in the water calorimeter in Figure 5.2.

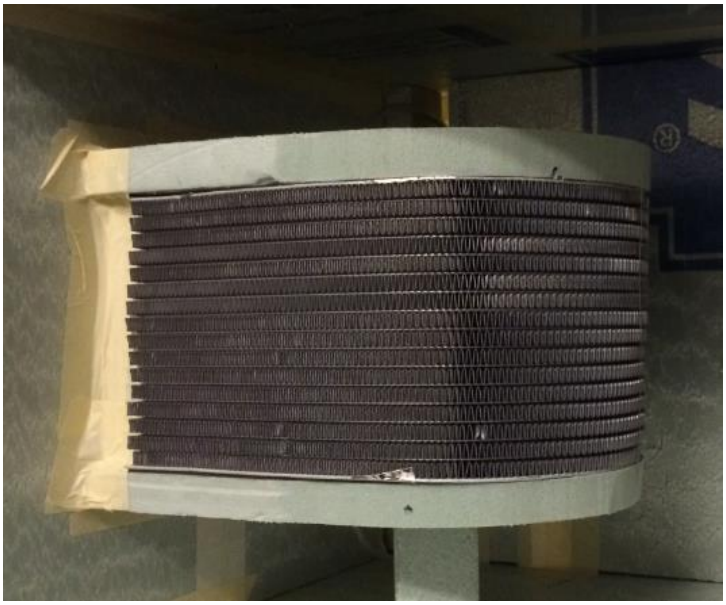

Figure 5.2: U-shaped MCHX installed in water calorimeter

The first thing to note about the data for the U-shaped MCHX is the energy balance is much better for this test when compared to the flat MCHX. The average over the entire test is 0.9% energy balance between the air side and liquid side measurements; this falls well below the 3% target for a good test. The test set points for the U-shape are also different than the test done for the flat. Only 16 points were taken for this shape with four liquid mass flow rates for each airflow rate compared to five for the flat. The trends in comparison to the flat remained the same; the heat transfer rate increased as airflow rate and liquid mass flow rate increased. The liquid side temperature change increased with airflow rate and decreased with mass flow rate. There were three points that didn't reach stability for this data set: 60 CFM/120 lb_m/hr, 60 CFM/135 lb_m/hr, and 70 CFM/140 lb_m/hr. This instability is commonly caused by the four airside TC's not meeting the stability criterial of ±1°F between them.

Table 5.2: Heat capacity of U-shaped MCHX from water calorimeter testing

Airflow Rate (CFM)	Liq Mass Flow Rate (lb_m/hr)	ΔT_{liq} (°F)	Energy Balance (%)	Q_{liq} (BTU/hr)
40	120	15.6	0.8	1875
40	125	15.3	0.9	1905
40	135	14.1	0.9	1899
40	140	13.8	0.6	1928
50	120	18.5	1.1	2214
50	125	17.6	0.8	2199
50	130	17.1	1.6	2218
50	140	16.1	1.0	2245
60	125	20.1	0.6	2515
60	140	18.4	0.8	2576
70	120	23.0	0.7	2753
70	125	22.2	1.3	2770
70	135	21.0	0.6	2833

5.1.3 ROLL

The roll MCHX is of the same construction as the flat just in a different shape. Shown in Figure 4.1 is the roll MCHX installed in the water calorimeter. The cardboard cap on the end of the roll blocks the air and forces it to flow across the fins. The white “wall” shown in the middle of the foam box is actually a honeycomb structure that helps to create uniform flow across the HX without adding much of a pressure drop. The MCHX was taped in place so there was no bypass air going around the HX. In the setup shown the side wall was put on and then the other two enclosures added, as described in Section 4.1.

The roll MCHX produced good stability during the test runs, having all 20 set points yield results. This test also showed good energy balance with an overall average

difference between airside and liquid side of 1.8%. Similar trends shown with the other two shapes can be seen in the data shown in Table 5.3. Heat capacity increased as airflow and liquid mass flow increased.

Table 5.3: Heat capacity of roll MCHX from water calorimeter testing

Airflow Rate (CFM)	Liq Mass Flow Rate (lb_m/hr)	ΔT_{liq} (°F)	Energy Balance (%)	Q_{liq} (BTU/hr)
40	120	15.2	2.4	1817
40	125	14.7	2.9	1836
40	130	14.1	1.7	1829
40	135	13.7	2.0	1842
40	140	13.3	2.2	1860
50	120	18.1	2.3	2175
50	125	17.4	1.6	2172
50	130	16.9	1.6	2195
50	135	16.3	1.3	2196
50	140	15.8	1.7	2214
60	120	20.5	1.3	2457
60	125	19.9	1.7	2487
60	130	19.2	1.5	2500
60	135	18.7	1.4	2521
60	140	18.2	1.8	2550
70	120	22.9	2.1	2743
70	125	22.2	2.0	2770
70	130	21.5	1.8	2798
70	135	20.9	1.7	2822
70	140	20.3	1.6	2840

5.1.4 EXPERIMENTAL HEAT TRANSFER CAPACITY SUMMARY

The heat transfer capacity data shown for each shape is summarized in Figure 5.3. The multiple data points at each airflow rate correspond to the different liquid mass flow rates. The flat geometry shows the highest heat capacity and the U-shape appears to have a slightly higher capacity than the roll. Airflow maldistribution is a term that represents airflow that isn't uniform. For the flat we have a very uniform airflow profile. For the U-shape and the roll the airflow will be maldistributed due to the shape. Quantification of the airflow maldistribution for the different shapes is shown in Section 5.2.

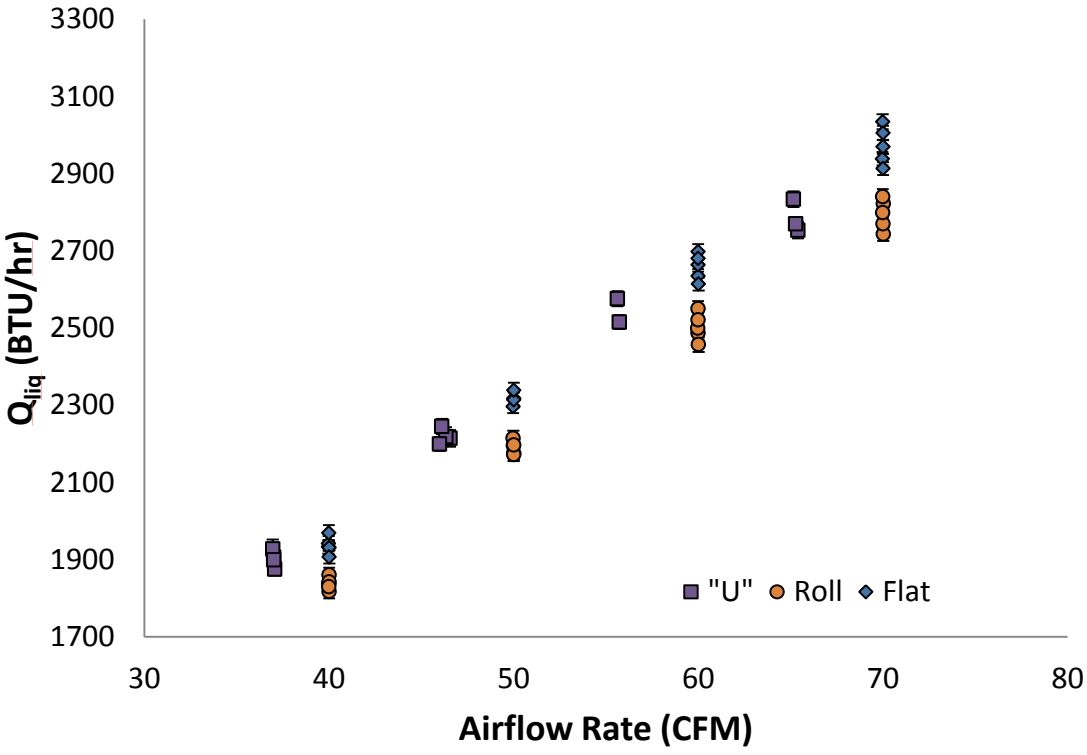

Figure 5.3: Heat capacity for each MCHX shape

The flat and the roll are the exact same construction, so they provide a good example to directly compare the effects of airflow maldistribution due to shape since their internal volumes and surface areas are identical. Considering only the points where both HX tests were stable the heat transfer capacity was on average 5.6% less for the roll than measured for the flat, ranging from 4.7% to 6.4%. This shows that heat capacity is affected when the airflow pattern around the heat exchanger is changed but the total airflow rate is held constant. The error bars were calculated using Equation [4-3]. The overall uncertainty was approximately ±1% for all heat capacities measured on the calorimeter with most of the uncertainty coming from the accuracy error in the RTDs.

5.2 Airflow Distribution

As discussed in Section 5.1.4 the airflow maldistribution is important to quantify to understand how the shape of the MCHX affects the overall heat transfer performance. As airflow maldistribution increases it is expected that the heat capacity of the coil should decrease. The measurement and analysis process for airflow will be shown for the flat HX first since it is the easiest to understand and explain.

Quantifying the airflow distribution is the second piece needed to connect the modelling in CoilDesigner™ with the effects of airflow maldistribution (MCHX shape). Several measurement techniques and averaging methods will be shown in the following sections.

5.2.1 FLAT

The flat shape is the easiest to measure and analyze because the flow distribution should be uniform. The flow should be perpendicular to the face of the HX as was shown in

Figure 3.5 and should be uniform across the HX. The first technique used to measure the airflow was a vane anemometer that was described in Section 4.2. The diameter of the sensor is just less than 4 inches so there isn't a lot of resolution in the data but it will give a general idea of the flows. The anemometer is shown in use in Figure 5.4.

Figure 5.4: Vane anemometer measuring flat MCHX

Air velocity measurements were taken at 12 locations along the length of the tubes. The 12 locations were overlapping by the radius of the anemometer. A schematic showing the overlapping measurement locations is in Figure 5.5. Top to bottom variation was assumed to be negligible during this experiment.

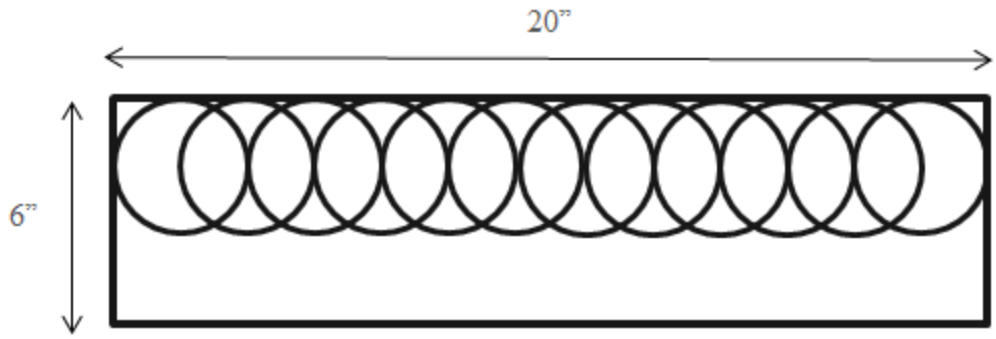

Figure 5.5: Vane anemometer measurement location schematic for flat MCHX

Velocities were measured for three different flow rates: 50, 75, and 100 CFM. The resulting local velocities are shown in Figure 5.6. As expected the velocity profile is very uniform across the face of the coil; within the uncertainty of the measurements.

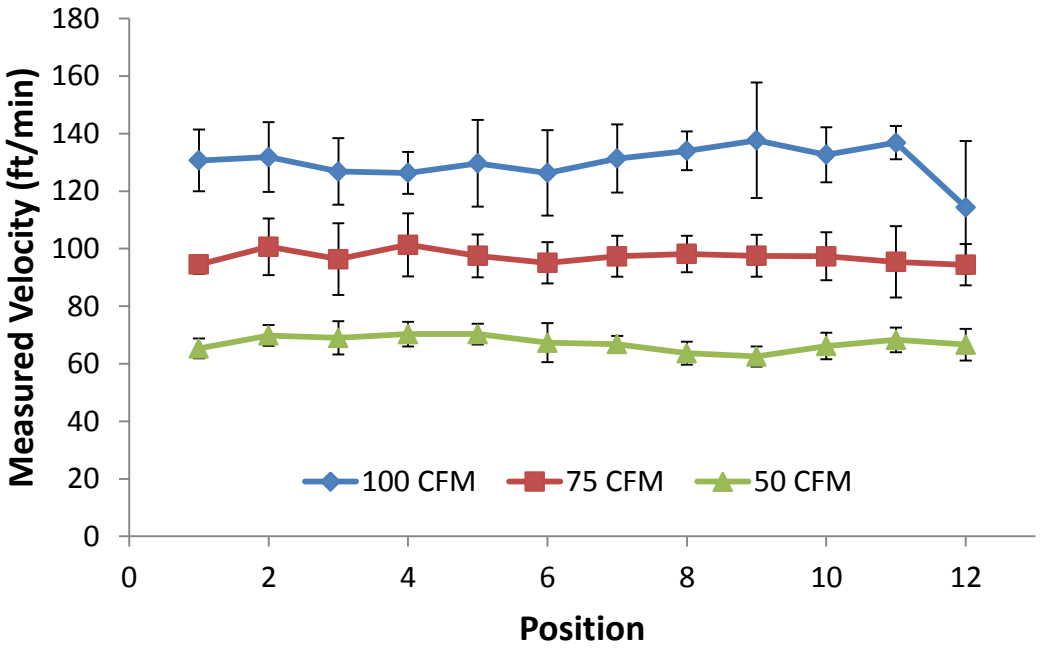

Figure 5.6: Local velocity measurements for flat MCHX using vane anemometer

The following calculations were made to show that the distribution doesn't change as the flow rate increased from 50-100CFM. Calculating a normalization factor based on the

maximum velocity will show the relationship between the three data sets. The calculation for normalization factor, F, is shown in Equation [5-3].

$$F = \frac{V_i}{V_{meas,max}} \quad \textbf{[5-3]}$$

Where V_i is an individual velocity measurement and $V_{meas,\ max}$ is the maximum local velocity measured for a given volume flow rate setting. The normalization factors for each airflow rate have been plotted in Figure 5.7. The points all collapse around 1 which shows good uniformity between measurement locations. This result also shows the velocity profile for the flat MCHX isn't affected by the airflow rate.

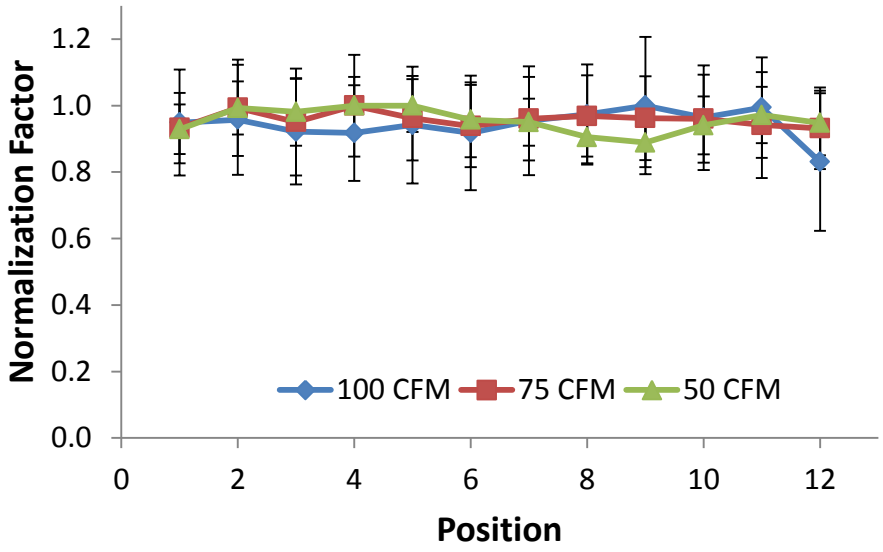

Figure 5.7: Normalization factors for flat MCHX velocity profile

In order to generate one profile from the three sets of measurements taken for different airflow rates, the three points were averaged for each position; the result is shown in Figure 5.8. The average normalization factors define the airflow profile for the flat

MCHX. The average normalization factor profile will eventually lead to the velocity profile for any given airflow rate.

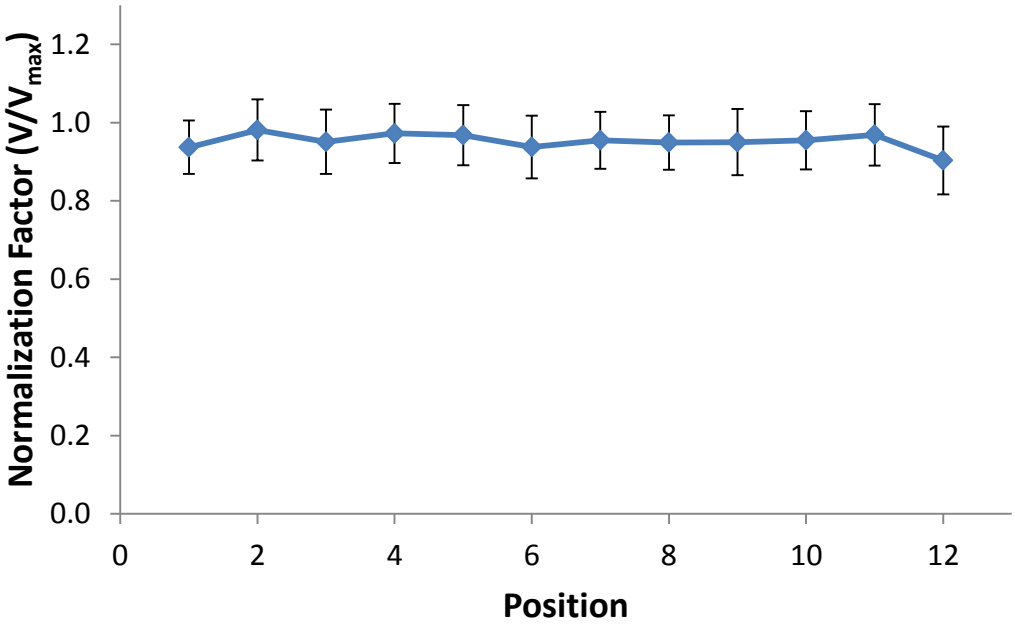

Figure 5.8: Average normalization factors used to characterize the profile of the flat MCHX

In order to develop a velocity profile that is balanced with the total airflow the measurement data needs to be manipulated using a series of calculations. Mass needs to be conserved so the individual mass flow rates need to add up to the total mass flow rate as shown in Equation [5-4]. Mass flow rates can be converted to volume flow rates by multiplying by density; Equation [5-5]. Volume flow rates can be converted to velocities by multiplying by area because the individual areas are the same; Equation [5-6]. The normalization factors previously calculated were determined based on the measured maximum velocity in that dataset. In order to accurately develop a profile using the measured data a new maximum needs to be calculated to properly scale the velocities so

mass balance is maintained. The result of combining Equations [5-4], [5-5] and [5-6] is shown in Equation [5-7], where V_u is the expected average velocity assuming uniform airflow. The total area is split into N segments of the same size; Equation [5-8]. The velocity of the air through each section, V_i, is calculated by multiplying the normalization factor by the maximum velocity as shown in Equation [5-9]. The normalization factors, F_i, come from the measurements taken with the anemometer but the maximum velocity will be calculated so the mass balance is satisfied. Combining Equations [5-7], [5-8] and [5-9] and solving for $V_{calc,max}$ yields Equation [5-10].

$$\dot{m}_1 = \sum_{i=1}^{N} \dot{m}_i \qquad \textbf{[5-4]}$$

$$\dot{m} = \rho \dot{\forall} \qquad \textbf{[5-5]}$$

$$\dot{\forall} = VA \qquad \textbf{[5-6]}$$

$$A_{Tot} V_u = \sum_{i=1}^{N} A_i V_i \qquad \textbf{[5-7]}$$

$$A_{Tot} = NA_i \qquad \textbf{[5-8]}$$

$$V_i = F_i * V_{calc,\ max} \qquad \textbf{[5-9]}$$

$$V_{calc,max} = \frac{V_u * N}{\sum_{i=1}^{N} F_i} \qquad \textbf{[5-10]}$$

Once the maximum velocity is calculated normalized local velocities can be calculated using Equation [5-9]. The result of this process for the flat MCHX is shown in Figure 5.9.

The velocity profiles shown in Figure 5.9 should agree with the measured velocity profiles shown in Figure 5.6. The only difference between these two profiles is that it has been scaled to conserve mass for the calculated velocities. This whole process allows the velocity profile to be compared to a uniform airflow condition by using the flow rate, total area, and number of segments.

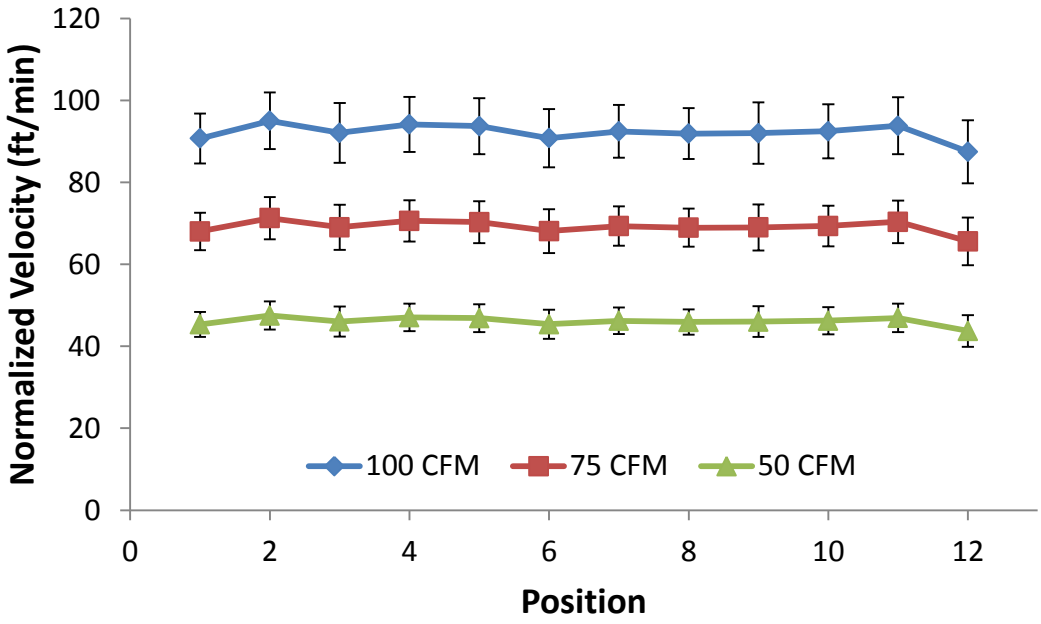

Figure 5.9: Normalized velocities for the flat MCHX

5.2.2 U-SHAPE

In the U-shaped MCHX it is expected that the velocity distribution will not be uniform. The airflow is expected to flow perpendicular to the face of the HX, as shown in Figure 3.7. The U-shape shown installed on the wind tunnel in Figure 5.10.

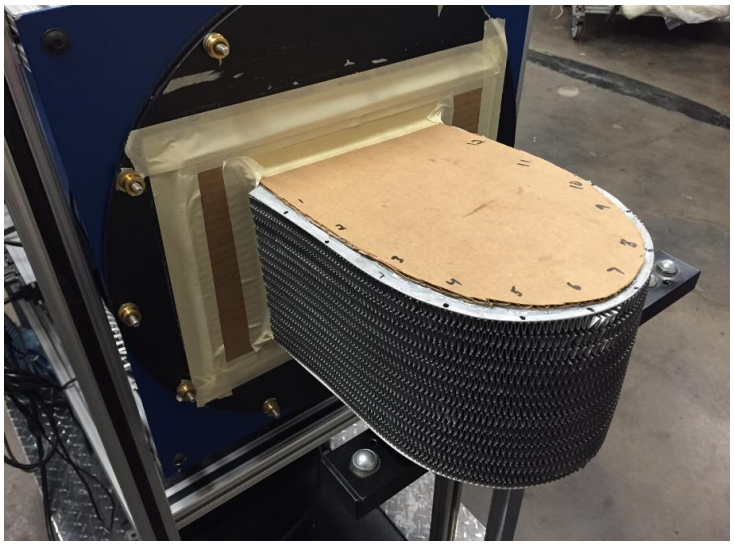

Figure 5.10: U-shaped MCHX installed on the wind tunnel for local velocity measurements

Velocities were measured at 12 locations using a ~4" vane anemometer. The process and instruments described in Section 4.2 were used for this test. The measurement location schematic is shown in Figure 5.11. The measurements are spaced apart by the radius of the anemometer. What is not shown is that the anemometer was mounted similarly to what was done for the flat geometry shown in Figure 5.4. It was aligned near the top to avoid interfering with the airflow by aligning along the center of the HX face. This inherently assumes negligible top to bottom variation.

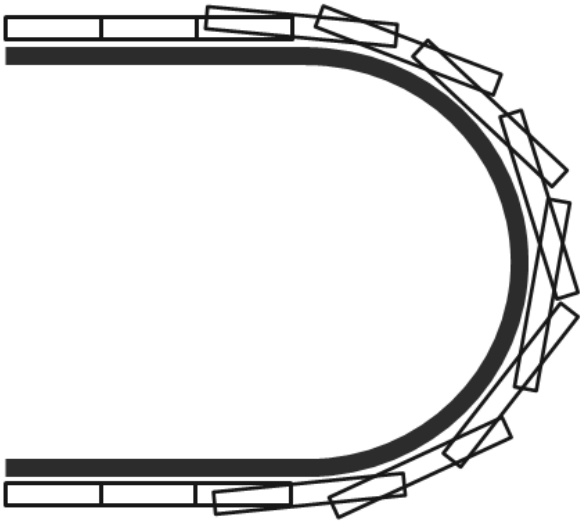

Figure 5.11: Vane anemometer measurement location schematic for U-shaped MCHX

The data analysis process for U-shaped MCHX was the same as that of the flat MCHX described in Section 5.2.1. The normalization factors ranged from 0.4 near the middle of the HX to 1 on either end. In Figure 5.12 the normalized velocity profile for the U-shape condenser is shown. As expected the local velocity decreased as the distance away from the wind tunnel blower increased. The profile was consistent despite changing airflow rates. This profile will be used to modify the model and determine the effects of maldistributed airflow on the U-shaped MCHX performance.

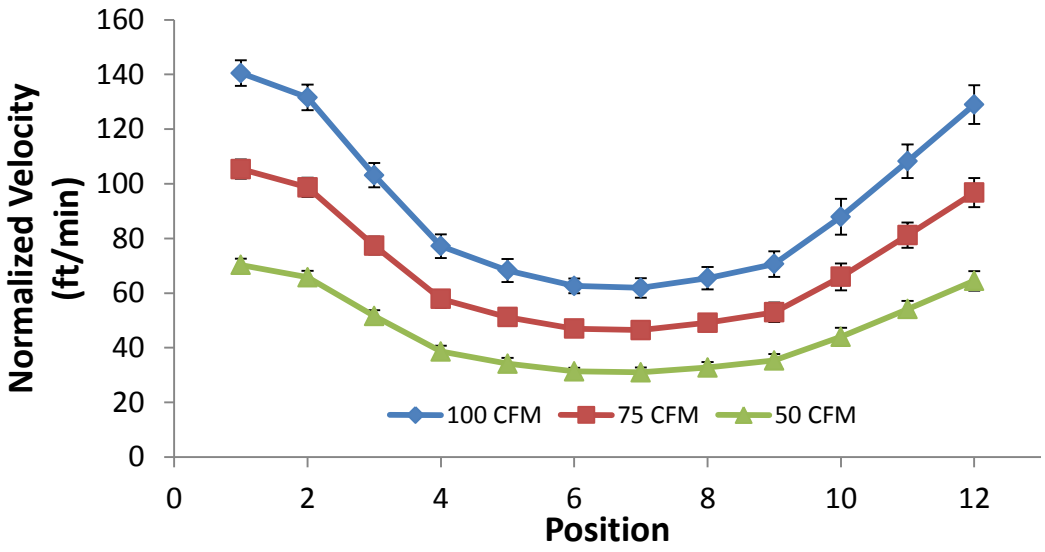

Figure 5.12: Normalized velocity profile for the U-shaped MCHX

5.2.3 ROLL

The roll MCHX is different than the other two geometries tested in that the main maldistribution is expected to occur along the axial direction of the roll, as described in Section 3.2. Since that was found to be the case, the data analysis process for this geometry was slightly different than for the previous two shapes. The 4" vane anemometer, a small hot wire anemometer and particle image velocimetry (PIV) were all used to measure the airflow for the roll MCHX.

5.2.3.1 Wind Tunnel and Vane Anemometer Measurements

The roll is shown installed on the wind tunnel in Figure 5.13. The four locations around the circumference of the HX where vane anemometer measurements were taken are positions 1, 5, 7 and 11 shown in the image.

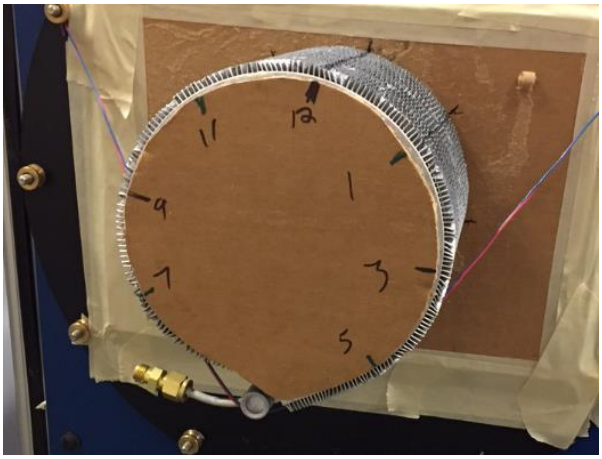

Figure 5.13: Roll MCHX installed on the wind tunnel for local velocity measurements

At each position two measurements were taken, one close to the open end of the roll and one towards the cardboard cap, effectively making two rings around the circumference of the HX. This is shown in Figure 5.14 where measurement locations 3-6 are out of the schematic on the underside of the HX. Due to the size of the sensor it is not possible to get more than two measurements along the roll axial length. It is worth mentioning the difficulty of measuring the velocity on the curved surface. Using a flat anemometer to measure airflow over the curved roll surface could allow air to bypass the anemometer and cause the measured value to be lower than actual. This was noted but isn't expected to significantly affect the results.

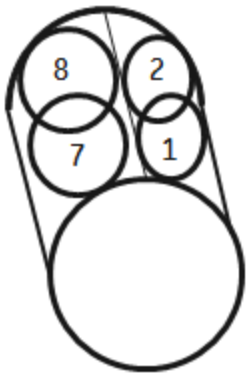

Figure 5.14: Vane anemometer measurement location schematic for roll MCHX

Similar to the wind tunnel testing for the other two geometries three airflow rates were tested. The measurement results for each rate are shown in Figure 5.15. The trend shows two distinct bands where the inner, closest to the open end of the roll, and outer measurements were taken. The process for calculating the velocity profile will be similar to that described in Section 5.2.1 for the flat shape.

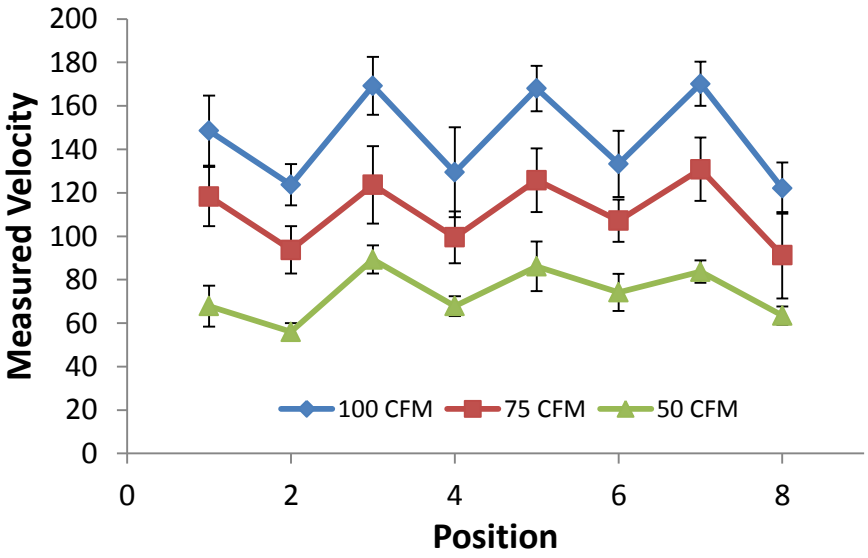

Figure 5.15: Local velocity measurements for roll MCHX using vane anemometer

Normalization factors were calculated and are shown in Figure 5.16. The normalization factors collapse very well along the same trend despite changing flow rates. The inner and outer bands are more distinct now and cause the data analysis to be slightly different than that of the flat and U-shapes.

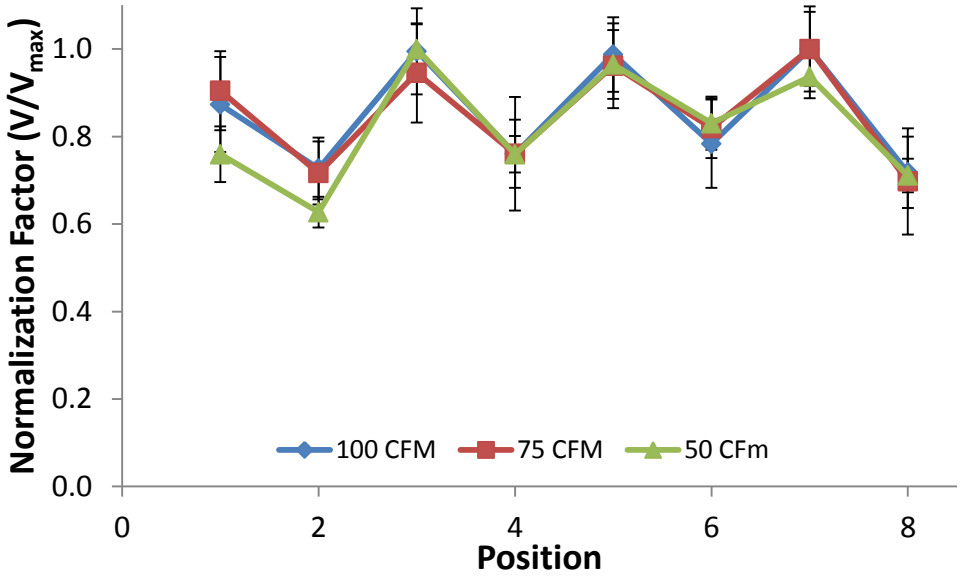

Figure 5.16: Normalization factors for roll MCHX velocity profile

The measurements for the roll MCHX are shown to be nearly uniform when grouped according to distance away from the fan or blower. The groupings are shown in Figure 5.17. The normalization factors for each flow rate were averaged together to yield one normalization factor for each position. The next step is to average the normalization factors in each band to get two normalization factors, one to describe the inner and one the outer band.

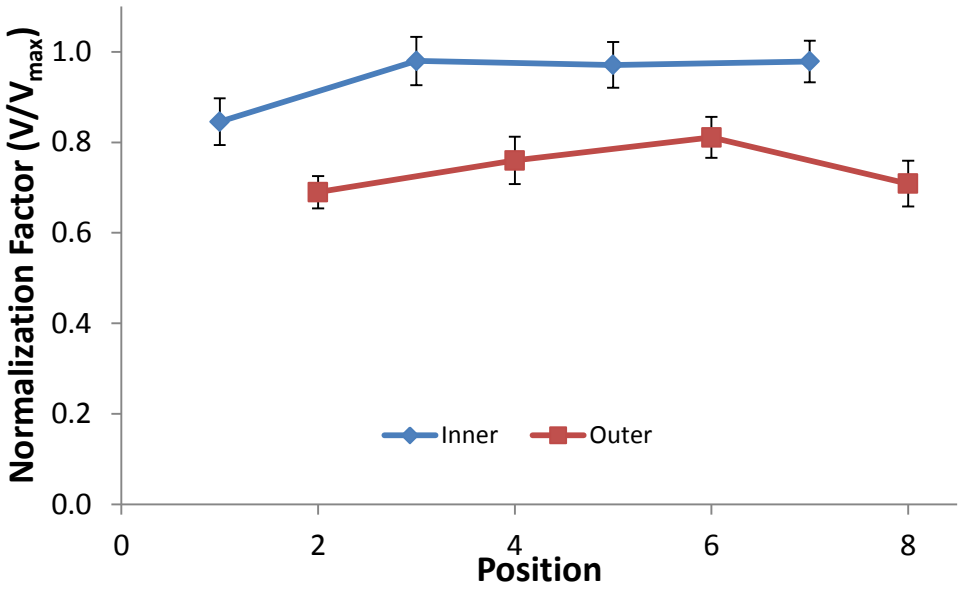

Figure 5.17: Normalization factors grouped by distance away from blower

The average normalization factors that describe each group were used to calculate a new normalized velocity profile using the same process described for the flat MCHX. A new maximum velocity was calculated that is scaled to ensure the conservation of mass when applying the normalization profile. The results are shown in Figure 5.18. This profile will be applied to the modelling software and the results compared with that of a uniform distribution assumption.

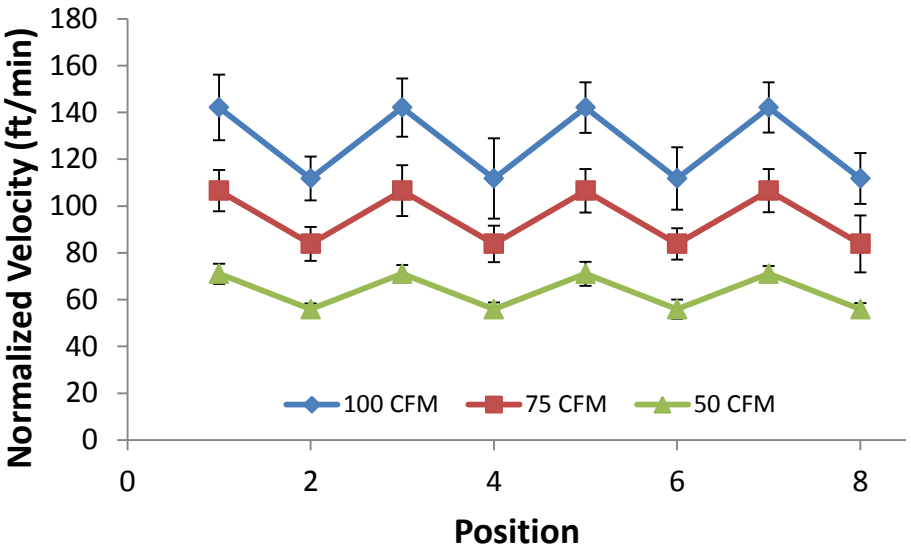

Figure 5.18: Roll MCHX normalized velocity profile

5.2.3.2 PIV Measurements

PIV can be used to measure the local airflow vectors around a louvered heat exchanger with a fine resolution. Measuring the velocity profile around finned heat exchangers has been a difficult problem creating challenges for designers for years. Without the ability to understand the effects of airflow around the HX it is difficult to optimize the design. Entire tubes may have low effectiveness because they are in an area with very low flow. PIV analysis has been shown to be able to quantify the velocity profile around a louvered fin HX by Yashar et al. (2008).

The setup used for this study is shown in Figure 4.8. The PIV results are displayed as a vector field and overlaid color map that indicate the flow within the grid. Each vector represents the average velocity measured within the vector's quadrant. More detail about the PIV equipment and techniques was discussed in Section 4.3. The PIV results for the

roll MCHX are shown in Figure 5.19. The seven images represent the velocity magnitude measurements taken at seven axial locations. Image one corresponds to the location closest to the fan and image seven is furthest from the fan, by the closed end. The images are each 1” apart and the roll is 6” tall to yield seven images. The velocity magnitude color scale is shown to the right of the images. The images shown portray the velocity magnitude in the color map and the vectors show direction in the two-dimensional plane.

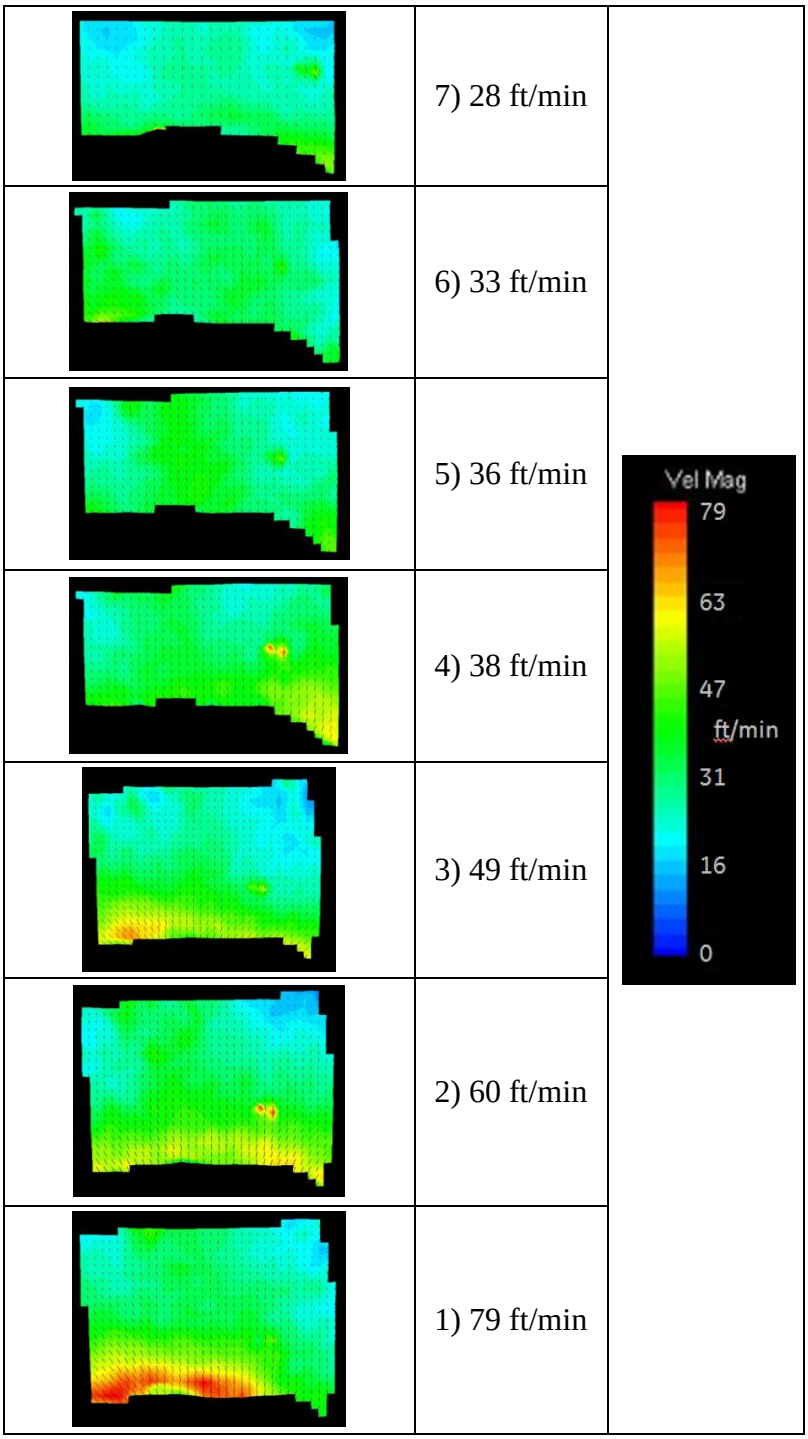

Figure 5.19: PIV results for the roll MCHX (1 closest to the fan; 7 furthest); velocity magnitude color scale shown on the right

Using this method will not provide a detailed quantitative result for the velocity profile, because PIV measurements cannot easily be taken around the circumference of the roll, but it was shown with the vane anemometer result that there wasn't much variation around the roll. Each image shows some of the curvature of the roll MCHX. The approximate middle of each image was selected as the point to obtain velocity data. The velocity estimates are shown next to the images in Figure 5.19.

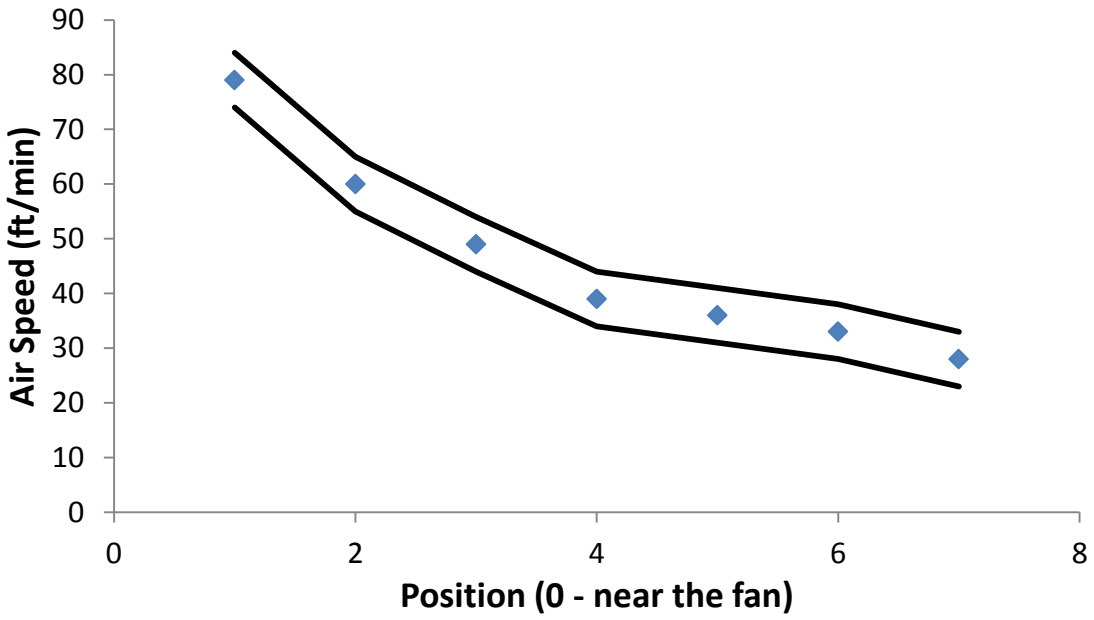

Figure 5.20: Air speed estimates for PIV measurements of the roll MCHX

The velocities have also been plotted in Figure 5.20 with a ±5 ft/min error displayed to account for the subjective nature of choosing the right location on the contour plot and assessing the color correctly. The trend in the plot is better represented by a logarithmic or power model than linear. This refutes the assumption made in Section 5.2.3.1 where the trend was assumed to be linear due to only two data points along the axis available for analysis. In Section 5.2.3.3 a hot wire anemometer will be used to corroborate the PIV

results. The increased resolution from PIV will allow for a more accurate airflow profile to be applied to the model.

5.2.3.3 Hot Wire Anemometer Measurements

The assumption after the vane anemometer measurements was local airflow speed decreased linearly as distance away from the fan increased for the roll MCHX. The vane anemometer was too large to be able to resolve a more detailed profile. The PIV analysis from Section 5.2.3.2 indicated the trend could be represented by a logarithmic or power model. The goal was to use hotwire anemometer measurements to confirm that result. Ten airspeed measurements were taken at each tube location for the roll; the averages for each tube are shown in Figure 5.21.

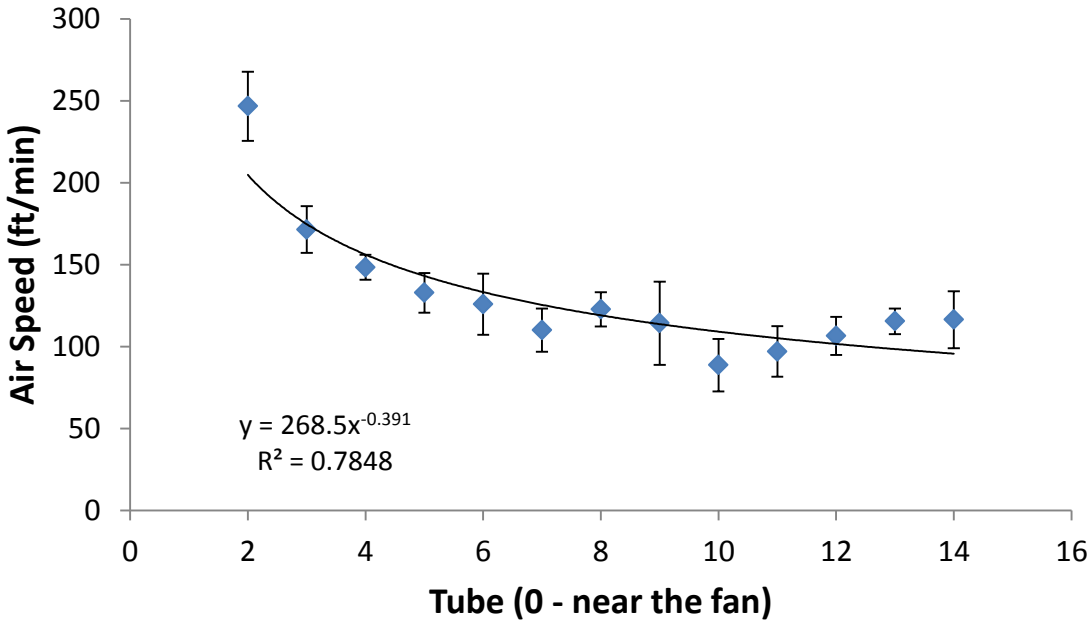

Figure 5.21: Local air speed measurements for roll MCHX taken with hotwire anemometer

For this range of air speed values the power function and logarithmic function both represented the data set well. The power distribution represented the data in Figure 5.21 slightly better according to the correlation coefficient. Using that equation and process shown in Section 5.2.1 to define the flat and U-shape airflow distribution, the profile was scaled to match any defined flow rate while conserving mass. This distribution will be applied to the model to determine the effect the airflow distribution has on the model, and if that effect corresponds with the experimental results from the water calorimeter.

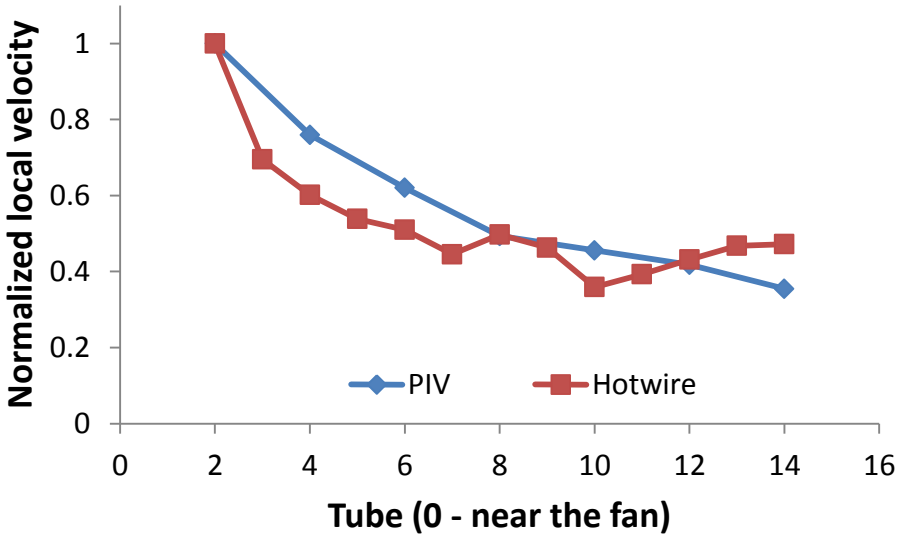

Figure 5.22: Normalized local velocities for roll MCHX comparing PIV and hotwire anemometer

There was a significant difference in magnitude of the PIV and hotwire velocity results, with the hotwire showing much higher local velocities. The PIV magnitudes were in good agreement with the vane anemometer magnitudes. The trend shown in Figure 5.21 appears to agree with the trend from the PIV results despite the shift in measured values.

The setup between the two tests was identical: only the measurement technique was different so it is unclear what caused the difference in results. The important thing is trend is the same, since this study is concerned with maldistribution. Despite what the actual values were the trend is what will be scaled to conserve mass for a defined flow rate. The local velocity data for PIV and hotwire was normalized to the maximum measured and the result is shown in Figure 5.22. This confirms that the trends are very similar.

6 PREDICTION RESULTS USING COILDESIGNER™

The HX liquid exit temperature and heat transfer capacity predictions are determined using CoilDesigner™ heat exchanger analysis software. An overview of CoilDesigner™, including the correlation used, input parameters, and validation study was shown in Section 2.4. CoilDesigner™ will be used to predict temperatures and heat capacity when the airflow is uniform and maldistributed. These results will show how the correlations respond to non-uniform airflow and hint at the levels of maldistribution that will affect the performance of a coil.

6.1 Flat

As was discussed in Section 5.1.1 for the experimental results, the flat MCHX is a baseline data point that can be used to benchmark the performance expectations of a coil as the airflow is modified to include maldistribution. That remains true as CoilDesigner™ is used to predict heat transfer capacity and refrigerant exit temperatures. The experimental data will be compared to the simulation results from CoilDesigner™.

All 19 inlet conditions from the water calorimeter experiment for the flat MCHX were input into CoilDesigner™ and the results for each condition were recorded. The results from the simulations are shown in Figure 6.1. The spread of heat capacity values is quite small when the airflow rate is low and gets larger as the airflow rate increases. This is

because more water flow is required to maximize the heat transfer capacity at higher airflow rates, giving the mass flow rate a larger effect. The spread between the liquid side temperature differences also correspond to increasing liquid mass flow rate.

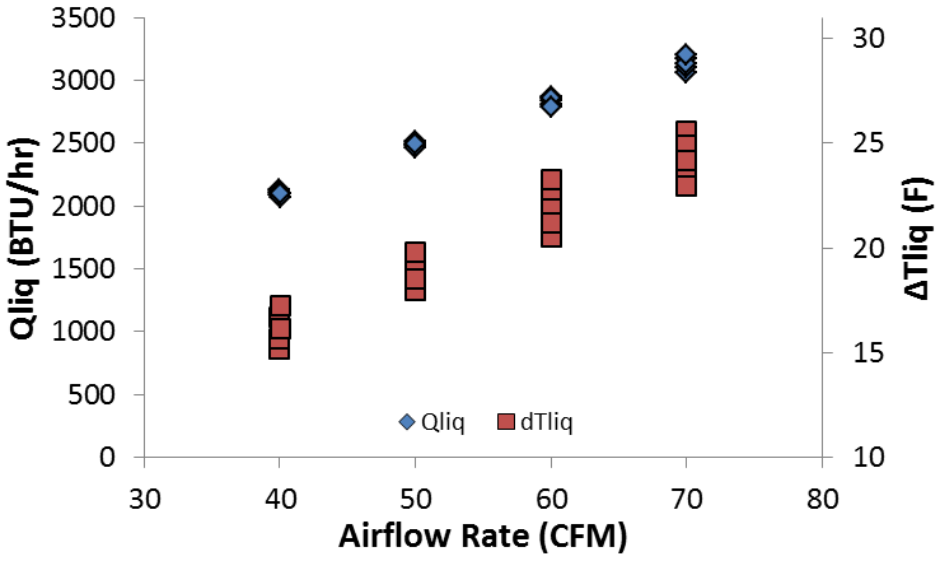

Figure 6.1: Heat transfer capacity and liquid side temperature difference for flat MCHX simulation

6.2 U-shape

The U-shaped MCHX simulation results shown in Figure 6.2 are for 12 of the 13 stable points tested in the water calorimeter assuming a uniform airflow distribution. Heat transfer capacity and liquid side temperature difference increased with increasing airflow rate. The points for both heat transfer capacity and liquid side temperature difference are clearly grouped by airflow rate. The small variations in temperature difference are caused by the mass flow rate set point at the same airflow rate. There is very little noticeable difference in the heat transfer capacity on this scale but if the scale were to be modified a

similar trend would be seen; the scale was chosen such that the two data sets didn't overlap and were easier to see.

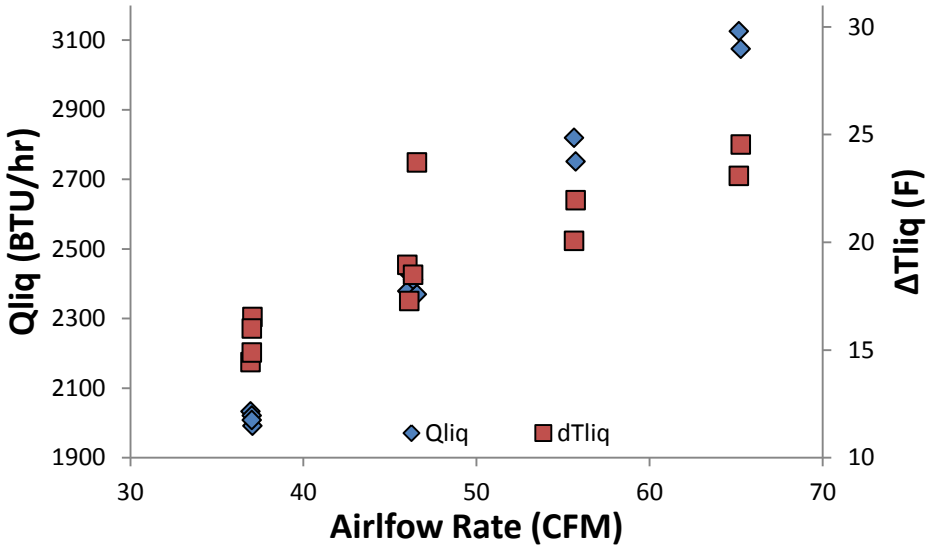

Figure 6.2: Heat transfer capacity and liquid side temperature difference for U-shaped MCHX simulation with uniform airflow

The 70 CFM/120 lb_m/hr calorimeter conditions produced an unsolvable function in a section of the MCHX. The error was "negative outlet pressure encountered" in one of the tube bends. This particular set of input parameters created a condition that the modeling software couldn't solve. The liquid side temperature difference for the 50 CFM/120 lb_m/hr point is significantly higher than the others points at 50CFM. This was the first data point taken on the calorimeter, so despite reaching stable conditions according to the air and liquid temperatures it is possible the calorimeter system had trouble on startup. This could explain the CoilDesigner™ issue with the 70 CFM/120 lb_m/hr conditions, as that was the second data point measured and could have also been caused by a calorimeter issue.

The simulation results shown in Figure 6.2 assume the airflow to be uniform across the face of the U-shaped MCHX. The actual air velocity profile for the U-shape was characterized in Section 4.3.1, and can be applied to the model in CoilDesigner™ using the procedure described in the appendix. The uniform airflow distribution would be expected to yield the highest possible heat transfer capacity and introducing any airflow maldistribution should result in a lower heat transfer capacity. In order to apply the velocity profile to the U-shape MCHX simulation, the airflow rate shown in Figure 5.12 was entered into CoilDesigner™.

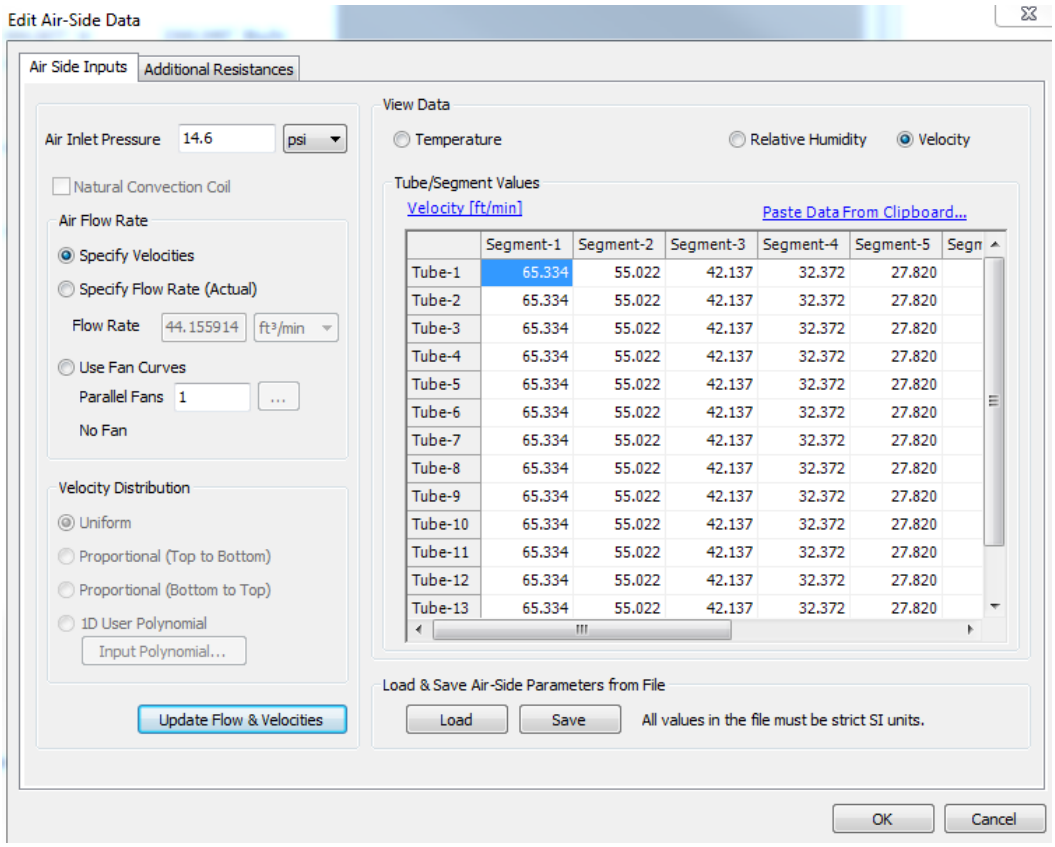

Figure 6.3: CoilDesigner™ air side parameter window showing velocity matrix for each segment and tube

Figure 6.3 shows the ability to edit specific velocities at different locations along the length of each tube. In the case of the U-shape, the airflow distribution is assumed to vary only along the length of the tube and remains constant from tube to tube. This means that each segment, one through ten, will have the same local velocity for each tube. CoilDesigner™ uses a text file to handle input conditions, and this file can be loaded with the velocity profile instead of entering each value by hand.

Table 6.1: Heat transfer capacity comparison for U-shaped MCHX with uniform airflow and vane anemometer profile

		Q_{liq} (BTU/hr)		
Airflow Rate (CFM)	Liq Mass Flowrate (lb_m/hr)	Uniform Profile	Vane Anemometer Profile	% difference
37	120	1992	1985	-0.4%
37	125	2008	2000	-0.4%
37	135	2020	2013	-0.4%
37	140	2033	2025	-0.4%
46	120	2369	2358	-0.4%
46	125	2378	2367	-0.4%
46	130	2412	2401	-0.5%
46	140	2428	2417	-0.5%
56	125	2751	2736	-0.5%
56	140	2819	2804	-0.5%
65	125	3074	3056	-0.6%
65	135	3125	3107	-0.6%
Average				-0.5%

The simulation comparison for heat transfer capacity between uniform airflow and the measured profile is shown in Table 6.1. Despite the significant difference in airflow through different portions of the MCHX the heat transfer capacity decreased by a maximum of 0.6%. A similar comparison was made for the liquid side temperature difference and the results are shown in Table 6.2. As shown by Equation [2-2] it is

expected that the simulation would show a similar change between heat transfer capacity and liquid side temperature delta, and it does. The 50 CFM/120 lb_m/hr, which was previously discussed to be a questionable data point, was the only data point that didn't follow this trend. This was the first data point taken on the calorimeter and the input conditions used for the simulation were set to match those of the calorimeter so it is possible that the calorimeter had an issue during the first run, despite the temperatures being stable. The simulation for that point was rerun multiple times and the result came back the same.

Table 6.2: Liquid side temperature difference for U-shaped MCHX with uniform airflow and vane anemometer profile

		ΔT_{liq} (°F)		
Airflow Rate (CFM)	Liq Mass Flowrate (lb_m/hr)	Uniform Profile	Vane Anemometer Profile	Temp Delta
37	120	16.5	16.5	-0.4%
37	125	16.0	15.9	-0.4%
37	135	14.9	14.8	-0.4%
37	140	14.4	14.4	-0.4%
46	120	23.7	19.9	-15.9%
46	125	19.0	18.9	-0.4%
46	130	18.5	18.4	-0.5%
46	140	17.3	17.2	-0.5%
56	125	21.9	21.8	-0.5%
56	140	20.1	20.0	-0.5%
65	125	24.5	24.4	-0.6%
65	135	23.1	23.0	-0.6%
Average				-1.7%

Overall, this result shows a fairly small effect, according to the simulation, on the performance of the coil when airflow maldistribution that is expected from normal operation is present.

6.3 Roll

The roll MCHX simulation results for all 20 stable conditions from the calorimeter testing are shown in Figure 6.4; assuming uniform airflow. As airflow rate increased heat transfer capacity and liquid side temperature difference both increased. This makes sense when consider the direct relationship between airflow rate and heat transfer capacity and liquid side temperature difference shown in Equation [2-2]; temperature difference, ΔT, increases and heat transfer rate, q, increases. Holding airflow rate constant and increasing the liquid mass flow rate increases the heat transfer capacity and decreases the liquid side temperature difference. This was the same result shown for the experimental calorimeter results in Section 5.1.3.

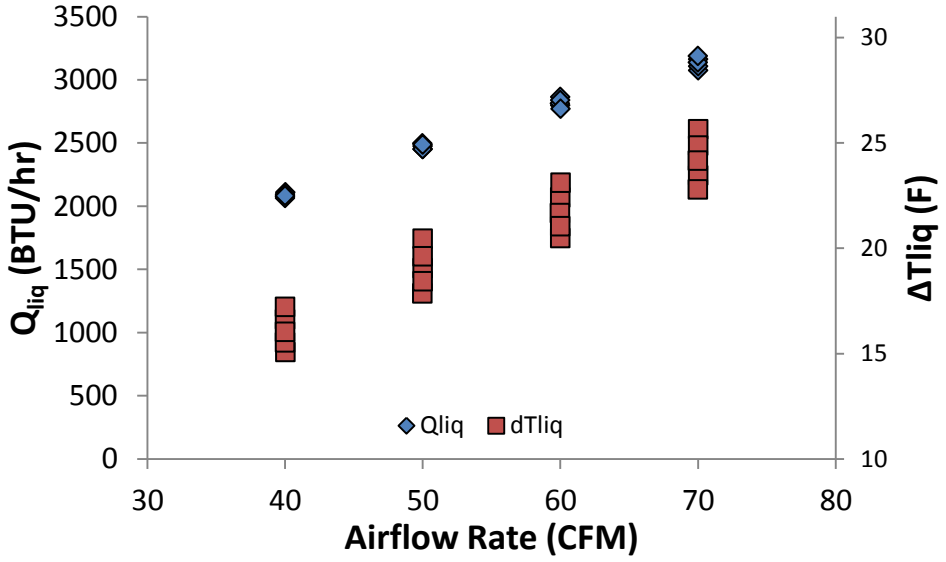

Figure 6.4: Heat transfer capacity and liquid side temperature difference for roll MCHX simulation with uniform airflow

Liquid side temperature difference and heat transfer capacity are directly related as shown in Equation [2-2], the percent difference between the uniform airflow simulation

result and any of the velocity profile results should be the same for both factors. This was shown in the simulation results for the U-shaped MCHX near the end of Section 6.2. To avoid redundancy only the heat transfer capacity rate will be presented.

Table 6.3: Heat transfer capacity simulation comparison between the uniform airflow profile, measured anemometer profile and linear profiles of different slopes

Q (Btu/hr)	% Difference in q			
Uniform Profile	Vane Anemometer Profile	Linear Max/Min = 2	Linear Max/Min = 5	Linear Max/Min = 10
2064	-0.2%	-0.7%	-2.5%	-3.7%
2076	-0.2%	-0.7%	-2.5%	-3.6%
2083	-0.2%	-0.7%	-2.3%	-3.4%
2095	-0.2%	-0.7%	-2.4%	-3.6%
2109	-0.2%	-0.7%	-2.4%	-3.6%
2451	-0.3%	-0.8%	-2.8%	-4.1%
2451	-0.3%	-0.8%	-2.7%	-4.1%
2475	-0.3%	-0.8%	-2.7%	-4.0%
2486	-0.3%	-0.8%	-2.7%	-4.0%
2497	-0.2%	-0.7%	-2.7%	-4.0%
2770	-0.3%	-0.8%	-2.9%	-4.4%
2798	-0.3%	-0.8%	-2.9%	-4.4%
2815	-0.3%	-0.8%	-2.9%	-4.3%
2839	-0.3%	-0.8%	-2.9%	-4.3%
2864	-0.3%	-0.8%	-2.9%	-4.3%
3075	-0.3%	-0.9%	-3.1%	-4.6%
3106	-0.3%	-0.9%	-3.0%	-4.6%
3139	-0.3%	-0.8%	-3.0%	-4.5%
3164	-0.3%	-0.8%	-3.0%	-4.5%
3188	-0.3%	-0.8%	-3.0%	-4.5%
Average	-0.3%	-0.8%	-2.8%	-4.1%

The airflow velocity profile for the roll isn't uniform, so the simulation was run again using the profile shown in Figure 5.18 that was measured with a 4" vane anemometer. The results for that simulation are shown in the second column of Table 6.3. That level of

airflow maldistribution resulted in an average decrease of 0.3% in heat transfer capacity for 20 conditions tested. When the capacity of each of these coils is over 2000 BTU/hr, 0.3% equates to 6 BTU/hr which is relatively insignificant.

Since the roll MCHX simulations show very small decreases in heat transfer capacity it is of interest to see what level of linear maldistribution it would take to affect the simulation results significantly. For the roll profile there were only two measurement locations using the vane anemometer because of the size of the anemometer and the short height of the coil. To increase the effect of the profile the resolution of the profile was increased and the profile assumed to be linear. The linear trend was used to estimate the roll profile for each tube, instead of only having two bands that covered seven tubes each. The profile would be divided into 14 sections; one per tube. The new profile would simulate a profile with the same mass flow rate but varying levels of maldistribution. The levels of maldistribution would be quantified by the ratio of maximum to minimum across the face of the coil. Since it is a linear profile the maximum to minimum ratio essentially defines the slope. Three levels of linear maldistribution were considered with slopes of 2, 5 and 10. All five velocity profiles applied to the roll MCHX simulation are shown in Figure 6.5.

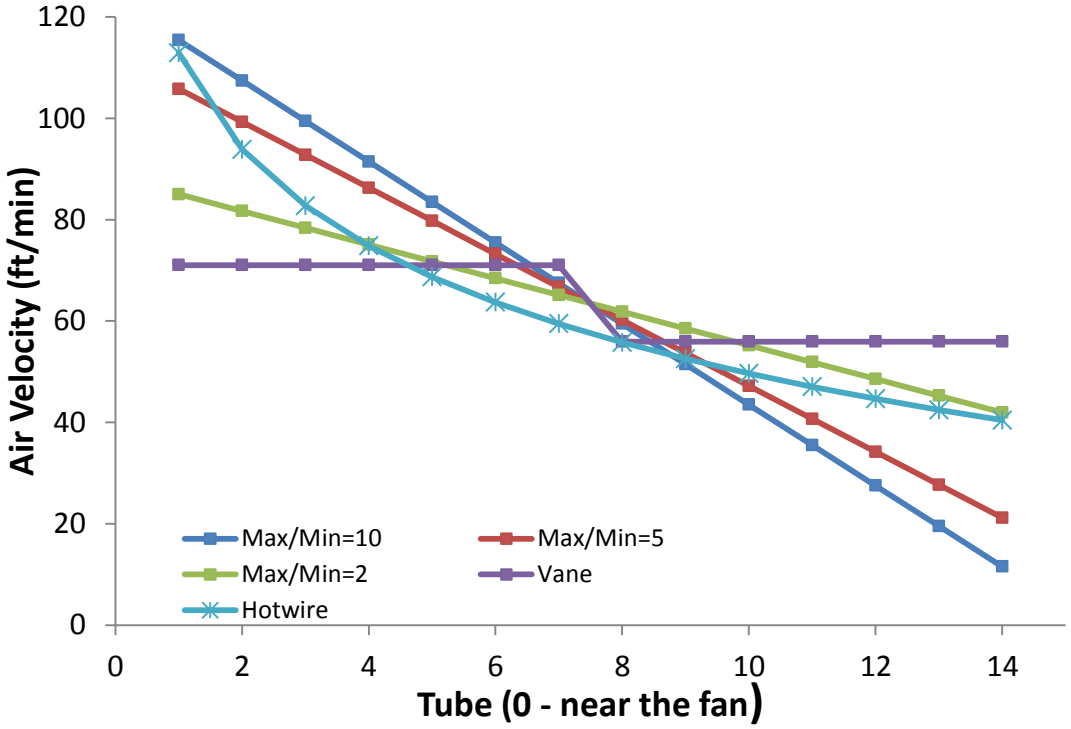

Figure 6.5: Air velocity profiles applied to the roll MCHX simulation

The results of the simulation for each velocity profile from Figure 6.5, as compared to the uniform profile simulation, are shown in Table 6.3. The average heat transfer capacity decrease for the max/min of two, five and ten were 0.8%, 2.8% and 4.1% respectively. All three had a greater effect than the measured profile from the vane anemometer. This result could indicate that the Chang and Wang correlation isn't designed to handle significantly maldistributed airflow or it could be a CoilDesigner™ limitation.

The last profile used in the simulation was developed using measurements from a hotwire anemometer. The hotwire anemometer has a much smaller footprint than the vane anemometer. The profile is shown in Figure 6.5 and the results are shown in Table 6.4. The average difference for the heat transfer capacity using the hotwire anemometer data

compared to the uniform profile was -1.5%. This shows a larger effect than the coarse profile measured with the vane anemometer but still isn't very significant.

Table 6.4: Simulation results for heat transfer capacity of the roll MCHX using the velocity profile measured using a hotwire anemometer

Hotwire Anemometer	
Q_{liq} (BTU/hr)	Q_{liq} % difference from uniform profile
2410	-1.7%
3016	-1.9%
2047	-1.4%
2087	-1.0%
2436	-1.6%
3165	0.0%
2747	-1.8%
3048	-1.9%
2815	-1.7%
2458	-1.6%
2411	-1.6%
3080	-1.9%
2035	-1.4%
2765	-1.8%
2447	-1.6%
2067	-1.3%
2789	-1.7%
2058	-1.2%
2719	-1.8%
3130	-1.8%
Average	-1.5%

7 COMPARISON OF EXPERIMENTAL WATER CALORIMETER RESULTS AND PREDICTIONS USING MORE DETAILED AIR VELOCITY PROFILES

Using standard correlations for louver fin geometry, heat capacity and refrigerant exit temperatures can be predicted for a coil of specified geometry. The results from the simulation are shown in Section 6. The simulation results are based on the best correlation currently available for a microchannel with louvered fins. The results from the simulation study will be compared to the experimental results described in Section 5.1. The assumption is made that the calorimeter data is accurate and the simulation is trying to predict the calorimeter result. The prediction errors will be calculated using Equation [7-1]; over prediction will be positive and under prediction will be negative.

$$\frac{Predicted\ Result - Calorimeter\ Result}{Calorimeter\ Result}\ x\ 100\% = Prediction\ Error \qquad \textbf{[7-1]}$$

7.1 Flat

The flat MCHX is taken as the baseline sample because the airflow pattern was shown to be uniform in Section 5.2.1, thus the simulation should yield the closest result to the experimentally measured calorimeter data because the modelling software assumes uniform flow. The liquid side temperature difference across the coil, ΔT_{liq}, and the heat transfer capacity will be directly compared for each set of initial conditions. Figure 7.1

shows the prediction error from the modeling software decreased as the airflow rate increased. This would indicate the correlation has a harder and harder time predicting the result from the calorimeter at lower airflow rates. The percent prediction errors between 5% and 8% translate to 3.5-6.5°F depending on the specified inlet condition.

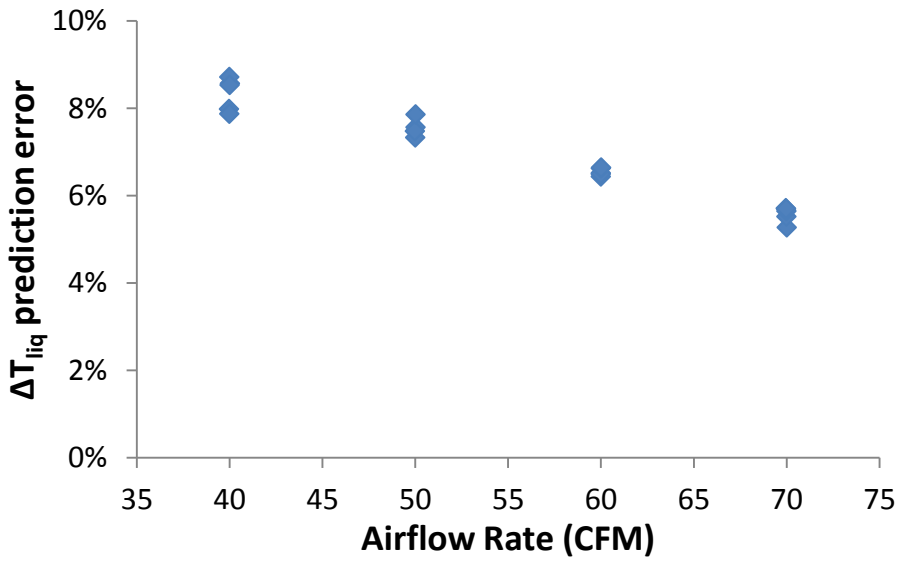

Figure 7.1: Liquid side temperature difference prediction error for the flat MCHX

The result shown for the heat transfer capacity prediction error in Figure 7.2 directly follows the temperature difference prediction error result. This is because of the relationship between the HX temperature difference and the heat transfer capacity, Equation [2-2]. The heat transfer capacity is predicted using the Chang and Wang (1997) correlation discussed in Section 2.3. The trend remained as shown for the temperature difference where the prediction error decreases as the airflow rate increases. For the sake of redundancy only the heat transfer capacity will be shown for the rest of the MCHX geometries.

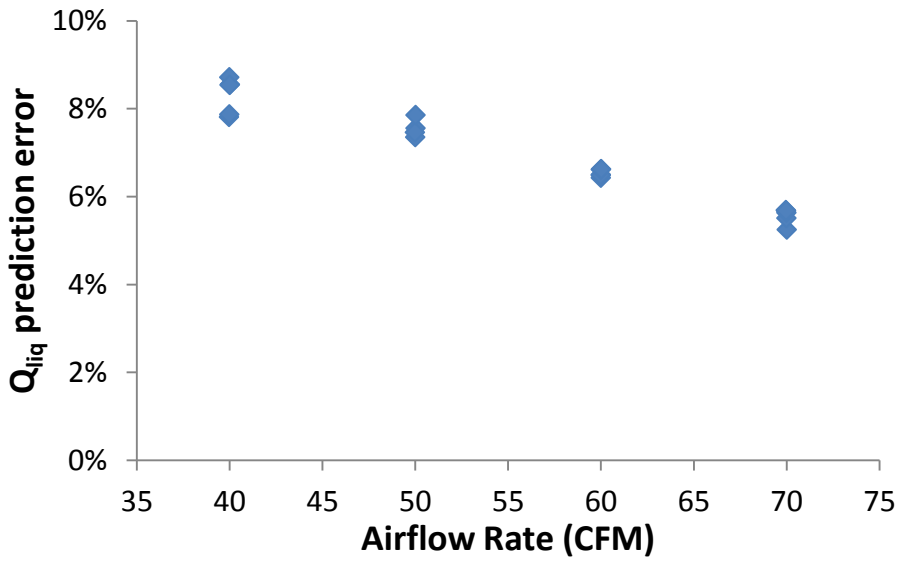

Figure 7.2: Heat transfer capacity prediction error for flat MCHX

Overall, this is a fairly good result for predicting the heat transfer capacity of the coil. Despite the fact that the Reynolds number is out of the recommended range for the correlation, as discussed in Section 2.3, the correlation did a pretty good job at predicting the result observed in the calorimeter given that the correlation was stated to predict 90% of the data within 15%.

7.2 U-shape

The U-shaped MCHX had a slightly higher prediction error than the flat MCHX, ranging from 5% to 11%, as shown in Figure 7.3. The distinct difference between the two data sets was the trend direction as it relates to the airflow rate. For the flat MCHX the prediction error decreased as the airflow rate increased; the opposite was true for the U-shape. It was expected that the trend between prediction error and airflow rate would

remain the same for all three geometries. The roll trend was similar to the flat, which will be discussed in Section 7.3.

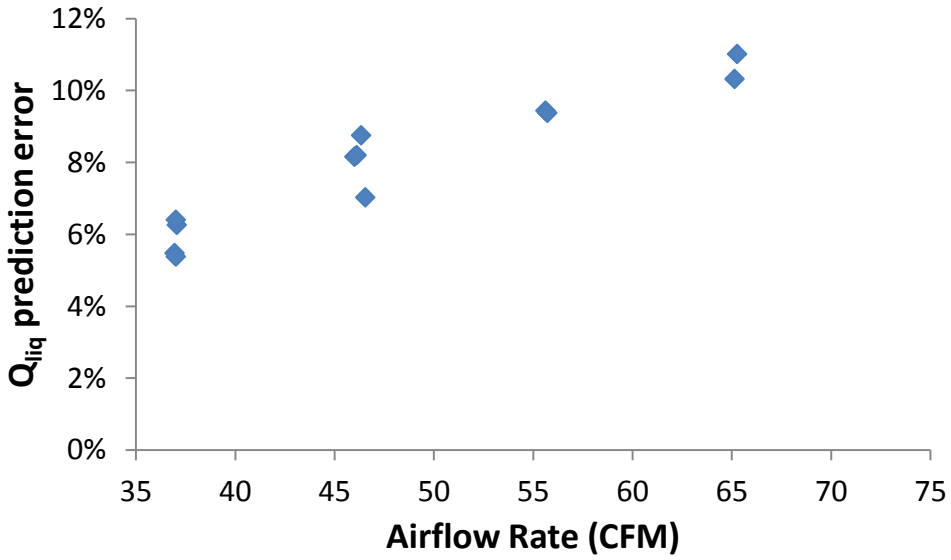

Figure 7.3: Heat transfer capacity prediction error for U-shaped MCHX

It was assumed there was a limitation in the correlation that increased the prediction error for the flat MCHX at low airspeeds, and that would drive the trend for all geometries. The trend shown in the U-shape result refuted that idea. Upon further investigation another trend became evident. The heat transfer capacity prediction error correlated well with the increase in relative humidity change across the heat exchanger. Shown in Figure 7.4 the flat MCHX data ranged from an RH delta of approximately 7.5% to 8.5%, whereas the results for the U-shape ranged from 5.5% to 11%. The correlation appears to under predict the heat transfer capacity at an increasing rate in cases where the inlet humidity was high. The U-shape calorimeter test was run at the beginning of the summer when outdoor humidity was high whereas the flat and roll calorimeter tests were done in

the middle of the winter with low ambient humidity. High outdoor humidity has been known to increase the humidity during calorimeter test for the system used in this study. This doesn't explain the correlation with the prediction error, however, considering the higher humidity inlet conditions were used for the prediction as well. It remains a point to be investigated at the end of this study.

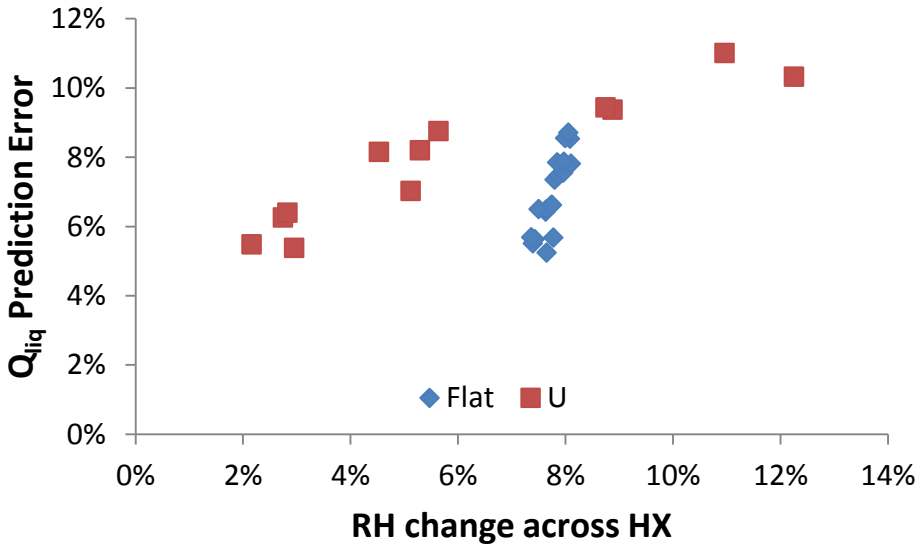

Figure 7.4: Heat transfer capacity prediction error as a function of change in RH across flat and U-shaped MCHXs

Shown in Table 6.1, are the prediction results for the U-shape when the vane anemometer profile was applied to the model. The net effect was, on average, a 0.5% decrease in heat transfer capacity. This would reduce the prediction error for the calorimeter result by the same amount, reducing the average across all inlet conditions from 8% to 7.5%. So applying the measured airflow distribution improved the prediction result by only 0.5%.

7.3 Roll

The roll MCHX calorimeter results will be compared to the prediction results from CoilDesigner™ shown in Section 6.3. Using the uniform airflow model, the roll shape yielded the highest heat transfer capacity prediction error among the different HX geometries. Figure 7.5 shows the prediction error ranged from 12% to 14%. The prediction error trends slightly downward as airflow rate increases, which agrees with the flat results.

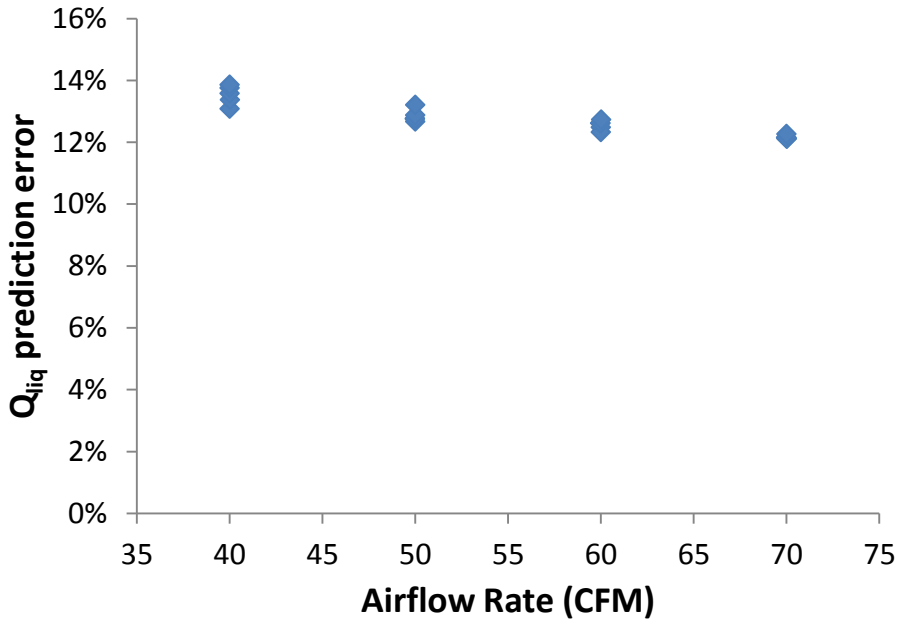

Figure 7.5: Heat transfer capacity prediction error for roll MCHX

It also seems there is some correlation between the relative humidity delta across the heat exchanger and the prediction error, Figure 7.6. This trend was apparent for both the flat and U-shape. This result agrees with the flat result best as the change in humidity across the heat exchanger was more consistent between test points as compared to the large

variation seen for the U-shape. Similar to the flat, the roll was tested in calorimeter in the middle of winter.

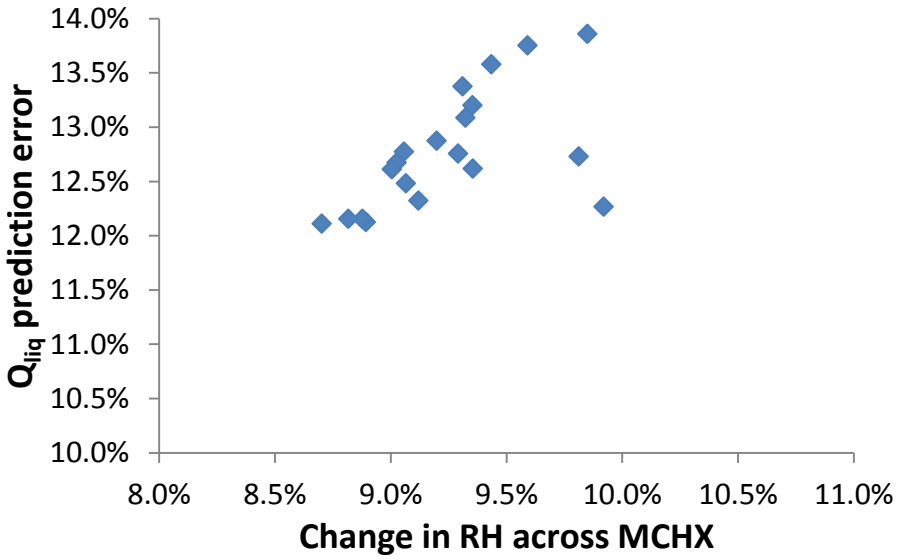

Figure 7.6: Roll MCHX heat transfer capacity prediction error shows correlation with increasing change in RH across the HX

The average prediction error for the heat transfer capacity of the roll MCHX using the uniform profile was 12.8%. Table 7.1 shows the effect of applying the velocity profiles from Section 6.3 to the model. The vane anemometer profile seems to have a small effect on the prediction error. On average error was only reduced by 0.3%. Since it was difficult to measure the profile using such a large anemometer, linear velocity profiles with increasing slopes were used. The intention was to determine how much airflow maldistribution it would take to have a drastic effect on the correlation. According to the results a velocity distribution with a slope of ten affected the model result by 4.7% when compared to the calorimeter result.

Table 7.1: Heat transfer capacity prediction error for roll MCHX

Q_{liq}(BTU/hr)	Q_{liq} Prediction Error				
Calorimeter	Uniform Profile	Vane Anemometer Profile	Max/Min = 2	Max/Min = 5	Max/Min = 10
1829	13.9%	13.6%	13.1%	11.3%	10.0%
1836	13.1%	12.8%	12.3%	10.3%	9.0%
1842	13.8%	13.5%	13.0%	11.0%	9.7%
1817	13.6%	13.3%	12.8%	10.7%	9.4%
1860	13.4%	13.1%	12.6%	10.6%	9.3%
2214	12.8%	12.5%	11.9%	9.7%	8.3%
2195	12.8%	12.5%	11.9%	9.7%	8.2%
2172	12.9%	12.6%	12.0%	9.8%	8.3%
2175	12.7%	12.4%	11.8%	9.6%	8.1%
2196	13.2%	12.9%	12.3%	10.1%	8.7%
2500	12.6%	12.3%	11.7%	9.3%	7.7%
2521	12.6%	12.3%	11.7%	9.4%	7.8%
2550	12.3%	12.0%	11.4%	9.1%	7.5%
2487	12.5%	12.2%	11.6%	9.2%	7.6%
2457	12.7%	12.4%	11.8%	9.4%	7.8%
2798	12.2%	11.9%	11.2%	8.8%	7.1%
2840	12.3%	11.9%	11.3%	8.9%	7.2%
2770	12.2%	11.8%	11.2%	8.7%	7.0%
2743	12.1%	11.8%	11.1%	8.7%	7.0%
2822	12.1%	11.8%	11.2%	8.7%	7.0%
Average	12.8%	12.5%	11.9%	9.7%	8.1%

The profile developed using hotwire anemometer measurements is shown in Figure 5.21. This profile was not included with the initial set of tests because it was unclear that a higher level of resolution would be required to accurately represent the airflow profile around the roll MCHX. After analyzing the PIV result it became clear the vane anemometer would not be adequate. It is expected the hotwire anemometer profile will yield a better prediction from the simulation than the profile developed using the vane anemometer. In Table 7.2 the average prediction of heat capacity for the hotwire

anemometer profile is shown to be 1.8% more accurate than the uniform profile assumption and 1.5% more accurate than the coarse profile measured with the vane anemometer.

Table 7.2: Average heat transfer capacity prediction errors for different airflow profiles

	Q_{liq} Prediction Error
Uniform Profile	12.8%
Vane Anemometer Profile	12.5%
Hotwire Anemometer Profile	11.0%

The velocity distribution doesn't appear to be a major source of difference between the measured and predicted capacity, since 11% error, 4% more than the flat, still exists even after correcting for the maldistribution. There are other things that weren't accounted for in the airflow distribution or modelling of the roll MCHX that could have added to the discrepancy between the roll and flat result. Shown in Figure 3.8, the roll construction actually overlaps itself. This wasn't accounted for in the airflow maldistribution. The overlap also wasn't accounted for in the model as it pertains to the proximity of those headers or tubes to each other and allowing heat transfer between them. This feature on the roll could significantly affect the prediction and will remain something to study further.

8 CONCLUSION

The goal of this study was to determine the effect shape has on the performance of microchannel heat exchangers in hopes that this technology can continue to be spread to other applications where limited space may require intricate designs. The study was conducted using a water calorimeter to validate prediction results from CoilDesigner™ modeling software. CoilDesigner™ uses the most recent heat transfer correlation for this type of HX, Chang and Wang (1997). Two of the MCHXs looked at in this study were identical in construction and geometry except for the shape they were formed into. The first was flat and the second was a roll shape. The flat had a measured capacity about 5% higher than the roll shape which showed some effect due to maldistributed airflow. Other geometric features of the roll could have caused this difference. The third shape looked at in this study has a slightly different construction and has a U-shape. The capacity of the U-shape was between that of the flat and roll coils.

Another goal of this study was to see how well the effects of unique shapes, or maldistributed airflow, on MCHX performance could be predicted by measuring the local airflow profile and feeding that information into the model simulation. Since the flat has uniform airflow across the face this was the baseline for CoilDesigner™ prediction error. CoilDesigner™ over predicted the liquid exit temperature and heat transfer capacity by 5-9% depending on the inlet conditions tested. One thing to note is the Chang and Wang

louver fin correlation is applicable for the range of Reynolds numbers based on louver pitch from 100 to 3000, but in this study the Reynolds numbers were below 50. Using the correlation outside its intended range is one source of error in the predictions but overall the results were within a favorable range.

Multiple airflow measurement techniques were used to quantify the airflow distribution of the different shapes: a vane anemometer, particle image velocimetry and a hot wire anemometer. The airflow profiles measured with the different techniques were used in combination with CoilDesigner™ to determine the accuracy of the prediction as it pertained to maldistributed airflow. The airflow measurement technique that best suited the roll was the hotwire anemometer measurements. Applying that profile to the CoilDesigner™ model yielded a 1.5% predicted decrease in the heat transfer capacity of the roll compared to the flat. The heat transfer capacity decrease would be expected to match the result from the calorimeter which was 5%. This could indicate a limitation of the Chang and Wang correlation, CoilDesigner™, an outside factor that has been neglected in this study or a combination of all three. In some of the studies previously done with this type of modelling a significant amount of work went into using correlation correction factors. In those studies each coil was tested and correction factors were used to improve the prediction before any optimization or modification was made. That was outside the scope of this study but could provide a significant amount of benefit to this study. Another area that could be investigated is two-dimensional airflow maldistribution; in this study only one-dimensional variation was considered.

Overall, these results indicate that maldistributed airflow may have only a small effect on the overall performance of the MCHX and the prediction techniques used in this study have a limited ability to accurately quantify the effects. More trials with samples of different size and construction would need to be conducted to make a more definitive statement.

9 RECOMMENDATIONS

In the present study many assumptions were made to simplify the velocity distribution measurements and modelling. The airflow maldistribution was only considered in the direction perpendicular to the airflow source. Going forward the prediction accuracy could improve if the entire face of the condenser was measured and a 2D profile applied to the CoilDesigner™ model.

Further work at compensating for unique geometric features, i.e. the roll MCHX overlap, in the modelling could also improve the results between CoilDesinger™ and the water calorimeter measurements. This will require measuring the airflow in that region but also looking at the effect of local heat transfer between the two layers of the tubing.

As was mentioned in the Past and Present Studies section of this paper, there is a study being done at Florida International University on a low Reynolds number correlation for louver fins. It would be interesting to see if the predictions using that correlation improve for the data in this study, given the Reynolds numbers in this study were below the recommended range for the Chang and Wang correlation.

There is a feature in CoilDesigner™ that allows for applying correction factors to each correlation used in the model. There are studies that outline a process for using these correction factors. The intent is to apply a correction factor to get closer to a measured

value from the calorimeter. Then use the software to make design changes using that correction factor as long as the construction of the coil doesn't change too drastically during simulation.

The last thing to recommend for this study is to measure and predict many more shapes to make a more definitive statement about the differences between the results. As this type of work continues strategies can be developed to handle unique geometries and save more time on the design side as the ability to predict heat exchanger performance improves.

REFERENCES

Achaichia, A., & Cowell, T. A. (1988). Heat transfer and pressure drop characteristics of flat tube and louvered plate fin surfaces. *Experimental Therma land Fluid Science*, 147-157.

CEEE. (2004-2016). CoilDesigner™. University of Maryland.

Chang, Y.-J., & Wang, C.-C. (1997). A generalized heat transfer correlation for louver fin geometry. *International Journal of Heat and Mass Transfer*, 533-544.

Ga Tech. (2014). *Design of Air-Cooled Microchannel Condensers for Mal-Distributed Air Flow Conditions.* Retrieved October 29, 2014, from Sustainable Thermal Systems Laboratory: http://stsl.gatech.edu/research-aircoupled.html

Gnielinski, V. (1979). New equations for heat and mass transfer in turbulent pipe and channel flow. *International Chemical Engineering*, 359-368.

Holman, J. P. (2001). *Experimental Methods for Engineers.* New York: McGraw-Hill.

Huang, L., Aute, V., & Radermacher, R. (2014a). A model for air-to-refrigerant microchannel condensers with variable tube and fin geometries. *International Journal of Refrigeration*, 269-281.

Huang, L., Aute, V., & Radermacher, R. (2014b). Design optimization of variable geometry microchannel heat exchangers. *15th International Refrigeration and Air Conditioning Conference at Purdue*, (pp. 1-10).

Keane, R. D., & Adrian, R. J. (1990). Optimization of Particle Image Velocimeters. *Measurement Science and Technology*, 1202-1215.

Khan, M. G., & Fartaj, A. (2011). A review on microchannel heat exchangers and potential applications. *International Journal of Energy Research*, 553-582.

London, A. L. (1980). A Brief History of Compact Heat Exchanger Technology. *Compact Heat Exchangers - History, Technological Advancement and Mechanical Design Problems* (pp. 1-3). Chicago: ASME.

Mehendale, S., Aute, V., & Radermacher, R. (2014). Principles of Refrigerant Circuit Optimization in Single Row Microchannel Condensers. *15th International Refrigeration and Air Conditioning Conference at Purdue*, (pp. 1-10).

Shah, R. K., & Sekulic, D. P. (2003). *Fundamentals of Heat Exchanger Design.* Hoboken: John Wiley & Sons.

Subramaniam, V., & Garimella, S. (2005). Design of Air-Cooled R-410A Microchannel Condensers. *ASHRAE Transactions*, 471-486.

Sunden, B., & Svantesson, J. (1992). Correlation of j- and f- factors for multilouvered heat transfer surfaces. *Proceedings of the 3rd UK National Heat Transfer Conference*, (pp. 805-811).

Webb, R. L., & Jung, S. H. (1992). Air-side performance of enhanced brazed aluminum heat exchangers. *ASHRAE Transaction 98*, (pp. 391-401).

Yashar, D., Cho, H., & Domanski, P. (2008). Measurement of Air-Velocity Profiles for Finned-Tube Heat Exchangers Using Particle Image Velocimetry. *International Refrigeration and Air Conditioning Conference* (p. 876). Purdue University.

NOMENCLATURE

Term	Description	Variable	Description
HX	Heat exchanger	Q	Heat capacity or heat transfer rate
MC	Microchannel	$\dot{m}$	Mass flow rate
MCHX	Microchannel heat exchanger	α	Surface area density
RTD	Resistance temperature detector	c_p	Specific heat
RH	Relative humidity	Δ	Change
		$\dot{V}$	Volume flow rate
Subscripts	**Description**	A	Area
liq	Liquid side	V	Velocity
air	Air side	U	Overall heat transfer coefficient
m	Mean	δ	Uncertainty/error
o	Out	T	Temperature
i	In	F	Normalization factor
Lp	Louver pitch	∀	Volume
p	Pitch	j	Colburn factor
l	Length	Re	Reynolds number
d	Depth	θ	Louver angle
f	Fin	F	Fin
u	Uniform	L	Louver
		T	Tube
		t	Thickness

COILDESIGNER™ LOCAL VELOCITY DISTRIBUTION PROCEDURE

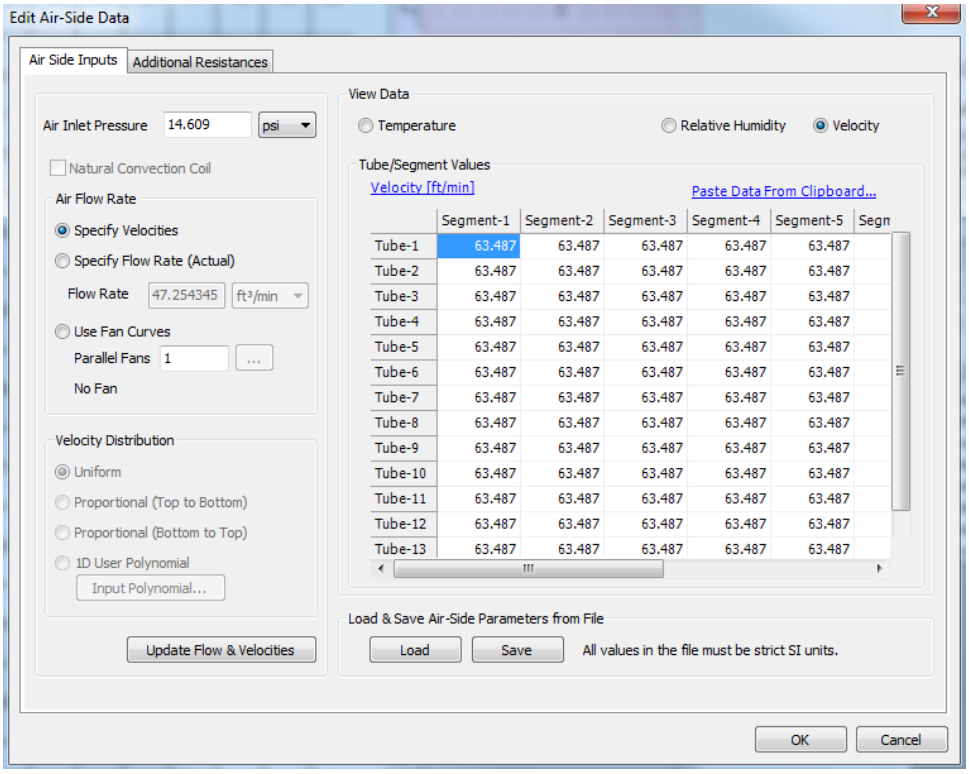

1. Under the projects menu select “Edit Air Side Parameters…”
2. Select “Specify Velocities” under the Air Flow Rate section
3. Select “Save” under “Load & Save Air-Side Parameters from File”
4. Open .txt file
5. Edit and save text file with local velocity profile (can copy and paste from excel)
6. Select “Load” under “Load & Save Air-Side Parameters from File”
7. Select .txt file that was saved in step 5
8. Select “Velocity” in “AirSideParameterSelectionForm” window
9. Select “Update Flow & Velocities”
10. Select OK
11. Warning reminding to click the “Update Flow & Velocities” button will pop up; select OK

CURRICULUM VITA

NAME:	Zachary Daniel Chapin
ADDRESS:	423 Kentucky Avenue Louisville, KY 40222
DOB:	Grand Rapids, MI – September 21, 1988
EDUCATION & TRAINING:	B.S., Mechanical Engineering University of Michigan 2009-2012